

Accurate method for ultralight axion CMB and matter power spectra

Rayne Liu,^{1,*} Wayne Hu,¹ and Daniel Grin²

¹*Kavli Institute for Cosmological Physics, Enrico Fermi Institute,
and Department of Astronomy & Astrophysics, University of Chicago, Chicago IL 60637*

²*Department of Physics and Astronomy, Haverford College,
370 Lancaster Avenue, Haverford, PA 19041, United States*

(Dated: December 20, 2024)

Ultralight axions (ULAs) with masses $10^{-33} \lesssim m/\text{eV} \lesssim 10^{-12}$ are well motivated in string-inspired models and can be part or all of the dark energy or the dark matter in this range. Since the ULA field oscillates at a frequency m that can be much larger than the expansion rate H , accurate and efficient calculation of cosmological observables requires an effective time averaged treatment. While these are well established for $m \gg 10H_{\text{eq}}$, the Hubble rate at matter-radiation equality, here we extend and develop these techniques to cover the mass range $10^{-33} \lesssim m/\text{eV} \lesssim 10^{-18}$. We implement this technique in a full cosmological Boltzmann code (AxiECAMB) with numerical precision sufficiently accurate for current and next-generation cosmic microwave background, as well as large-scale structure data analysis. New effects including the time averaging of metric perturbations and hydrostatic equilibrium of the effective fluid result in many orders of magnitude improvements for power spectra accuracy over some previous treatments such as AXIONCMB in some extreme regions of parameter space and order unity changes of the ULA effects near ΛCDM models. These improvements may impact the model parameters that resolve various tensions in ΛCDM at a comparable level.

I. INTRODUCTION

Cosmic microwave background (CMB) anisotropy measurements have facilitated the establishment of the Λ cold dark matter (ΛCDM) model as the standard model for cosmology [1–3]. Additional evidence for this paradigm comes from inferences of cosmic acceleration by Type Ia supernovae, as well as surveys probing the clustering of galaxies, baryon acoustic oscillations and weak gravitational lensing (e.g. [4–9]).

Despite these successes, the ΛCDM model is incomplete. The microphysical nature of the dark matter and dark energy remains unknown. Outstanding unresolved challenges to this paradigm also persist, such as the $\sim 5 - 6\sigma$ tension between CMB and Cepheid-supernovae inferences of the Hubble constant H_0 (e.g. [10]; cf. [11]), the small discrepancy between values of the amplitude of structure parameter $S_8 = \sigma_8 \sqrt{\Omega_m}/0.3$ inferred from the CMB and weak lensing measurements (e.g. [7–9]), and differences in the relative distance measures between supernovae, baryon acoustic oscillations and the CMB [5, 6]. These tensions may indicate a more complicated dark sector (see [12, 13] and references therein).

Some theoretical resolutions to these issues invoke new fundamental pseudo-scalar fields with extremely low mass scales ($10^{-33} \lesssim m/\text{eV} \lesssim 10^{-12}$), where m is the mass of the ultralight field and we set $c = \hbar = 1$ throughout. The existence of such fields is motivated by considerations in string-inspired models, where new gauge fields on compactified extra dimensions acquire mass through nonperturbative interactions and have pseudoscalar cou-

plings, like the axions which resolve the strong \mathcal{CP} problem of the standard model of particle physics; these fields are thus usually referred to as ultralight axions (ULAs). This has given rise to the idea of an *axiverse* [14–19], in which many such particles exist with a log-flat distribution of masses. Axion mass values may be even higher than $m \gtrsim 10^{-12}\text{ eV}$ and one of these particles could be the QCD axion [16], but we would then not classify them as ultralight. Similar dynamics occur for ultralight vector dark matter or dark photon (e.g. [20, 21]).

Such fields are initially cosmologically misaligned from their vacuum, and begin to oscillate coherently once $m \sim H \equiv d \ln a/dt$, diluting thereafter as a^{-3} in density, where a is the usual cosmological scale factor, and behave as dark matter. The Hubble rate at matter-radiation equality in ΛCDM ($H_{\text{eq}} \sim 10^{-28}\text{ eV}$) therefore approximately partitions ULAs into heavier ones that behave like dark matter on large scales and lighter ones that behave as dark energy at least during the initial phase of structure formation [22–24]. ULAs could thus contribute to some or all of the dark matter or energy. In the dark matter regime, ULAs could resolve a number of observational challenges to the ΛCDM cosmological paradigm on small scales [25], such as the *missing satellites* problem in the Local Group, the *too big to fail* problem, and the *cusp-core* problem with density profiles of low-mass galaxies [26–29].

ULAs have distinct cosmological signatures, altering the time evolution of the Hubble parameter, and affecting the evolution of density fluctuations in the universe. The macroscopically large de Broglie wavelengths of ULAs would suppress the growth of density fluctuations on small scales, making them an example of fuzzy dark matter (FDM) [30, 31]. As a component of the dark matter, ULAs can alter the acoustic peaks and the

* rayneliu@uchicago.edu

early integrated Sachs-Wolfe (ISW) effect in the CMB, carry isocurvature perturbations [32], contribute to an early dark energy component [33, 34], and alter the matter power spectrum. ULAs could thus alleviate the S_8 tension [35].

Cosmological data thus offer a powerful probe of the ULA possibility, with promising opportunities for experimental tests, e.g. ongoing and future CMB, galaxy clustering, and weak lensing data from the CMB-S4 experiment [36], the Rubin Observatory [37–39], the Euclid satellite [40], the DESI survey [41], and many others. To turn this data into robust ULA constraints, one must sample the likelihood function, comparing ULA model predictions to data. This requires rapid and accurate calculation of observables including CMB and matter power spectra.

For $m \gg H_0$, the field oscillates on a time scale much faster than that which cosmological observables evolve, making it numerically challenging to efficiently and accurately make theoretical predictions for the impact of ULAs. Boltzmann codes (such as AXIONCAMB [42] and AxICLASS [33]) used to impose current state-of-the-art constraints to ULAs address this timescale problem using an effective fluid approximation (EFA) that tracks the effective average of axion variables over oscillation cycles [30, 43], essentially employing a WKB-type approach.

Use of this approximation leads to numerical artefacts in mode evolution and observables [44]. The artefacts induced specifically by the EFA were found to be below the precision required for *Planck* data analysis but could introduce biases to parameter inferences in the future (e.g. from ongoing and upcoming experiments like the Simons Observatory or CMB-S4, respectively). AXIONCAMB has some additional numerical artefacts, some of which were addressed in the update from version 1.0 to 2.0, and others of which are discussed here.

A new algorithm was developed in Ref. [45], which refines the corresponding theoretical predictions to sub-percent accuracy without loss of computational speed for $m \gg 10H_{\text{eq}}$. This algorithm works by following the exact Klein-Gordon (KG) equation at background and perturbation level for at least a few cycles, and then matching the EFA variables to their effective time averages (ETAs) at a switch point. The ETA matching is constructed to exactly obey conservation laws, yielding optimized functional forms for EFA equation-of-state parameter and sound speed.

In Ref. [45], only $m \gg 10H_{\text{eq}}$ cases were considered, for which the ULA time averages need not account for the back reaction on metric fluctuations. The resulting differences from Λ CDM do not change CMB observables. The new EFA approach was applied in Ref. [46] to compute matter power spectra and halo-model observables in ULA models containing two light fields, inspired by the axiverse scenario. The method was also implemented in the CLASS Boltzmann codebase [47] in Ref. [48] again neglecting the metric effects when applied to the $m \ll 10H_{\text{eq}}$ regime.

An alternative approach was presented in Refs. [49–51]. There, fluctuations are factored into a smoothly evolving and oscillating component, with a specific phase-matching prescription applied at the onset of rapid oscillations, when numerical challenges emerge. Here again the techniques focused on the $m > 10H_{\text{eq}}$ regime.

Our work yields the first ULA Boltzmann code that is accurate and efficient for the ULA background and perturbations over a broad range of masses $10^{-33} \lesssim m/\text{eV} \lesssim 10^{-18}$. We develop and extend the effective methods of Ref. [45] to the $m \lesssim 10^{-25}$ eV regime and implement them in a new code, AxiECAMB¹ (Axion Effective-method in CAMB²) as a successor of AXIONCAMB. In this regime there are a number of additional effects due to the impact of the ULA on metric fluctuations and their behavior well below their cosmologically large Jeans scale.

We begin in Sec. II, where we explain the elements of the effective method: Klein-Gordon field solutions until a given switch epoch $m/H \approx 10$, their effective time average at the switch, and their evolution as an effective fluid thereafter. We discuss the impact of the ULA on CMB and matter power spectra in Sec. III and show that AxiECAMB is sufficiently accurate for current and next-generation surveys.

Technical issues are detailed in a series of Appendices: comparisons to previous work (A) including AXIONCAMB and fitting functions in the FDM regime; Klein-Gordon field solutions (B), including methods for predicting the oscillatory phase for $m \lesssim 10H_{\text{eq}}$; effective time averaging of variables (C), including metric perturbations; effective fluid construction (D), including the quasi-static limit for perturbations well under the Jeans scale; and CMB implementation (E), including their response to ULA oscillations and the impact of effective sources at the switch.

We discuss all of these results in Sec. IV.

II. EFFECTIVE METHOD FOR ULAS

Here we establish our effective method for ULAs to linear order in perturbation theory. We first briefly review the behavior of the Klein-Gordon system when the mass time scale becomes much shorter than the Hubble time (KG; Sec. II A). Extending the methods of Ref. [45], we then construct an effective time average (ETA; Sec. II B) of the ULA and metric variables at some appropriate switch time (henceforth “the switch”) and thereafter evolve this time average using an effective fluid approximation (EFA; Sec. II C). We address the choice of switch time and CMB sources in Sec. II D, in particular for cases where $10^{-28} \lesssim m/\text{eV} \lesssim 10^{-25}$.

¹ <https://github.com/Ra-yne/AxiECAMB>

² CAMB: <http://camb.info>

For testing the accuracy of our effective method here and below, we take as our fiducial model a cosmology with *Planck* baseline parameters $\Omega_b h^2 = 0.0224$, $\sum m_\nu = 0.06$ eV, $H_0 = 67.36$ km/s/Mpc [52] in a spatially flat cosmology. In the presence of ULAs with $m/H_0 \geq 10$, we replace the cold dark matter density $\Omega_c h^2$ with the total dark matter $\Omega_{\text{DM}} h^2 = \Omega_c h^2 + \Omega_{\text{ax}} h^2 = 0.12$. When $m/H_0 < 10$, ULAs behave as dark energy (DE), hence we parametrize its abundance instead with $f_{\text{DE}} \equiv \Omega_{\text{ax}} h^2 / \Omega_{\text{DE}} h^2$, where $\Omega_{\text{DE}} h^2 = \Omega_\Lambda h^2 + \Omega_{\text{ax}} h^2$ and leave $\Omega_c h^2 = 0.12$. In this section we will take $m = 10^{-27}$ eV and $f_{\text{DM}} = 1$ as our fiducial example unless otherwise specified.

A. Klein-Gordon Oscillations

The ULA field ϕ evolves via the Klein-Gordon equation $\square\phi = -V'$. We adopt the common assumption that the field is sufficiently close to its minimum that the quadratic approximation $V(\phi) \approx m^2\phi^2/2$ applies, and the background evolution becomes

$$\ddot{\phi} + 2\frac{\dot{a}}{a}\dot{\phi} + a^2 m^2 \phi = 0, \quad (1)$$

where overdots denote conformal time derivatives $d/d\tau = ad/dt$, and a is the usual cosmological scale factor. Once the Hubble rate $H = d \ln a / dt$ drops below the mass, the background field oscillates and H can become much smaller than the frequency m by the present for ULA masses of interest.

For spatial perturbations $\delta\phi$, we study the Fourier space evolution in synchronous gauge:

$$\ddot{\delta\phi} + 2\frac{\dot{a}}{a}\dot{\delta\phi} + (k^2 + a^2 m^2)\delta\phi = -\frac{\dot{h}}{2}\dot{\phi}, \quad (2)$$

where k is the comoving wavenumber and h is the fluctuation in the trace of the spatial metric. To complete the metric perturbations, we will use the spatial curvature η and the shear of the local expansion $\sigma = (\dot{h} + 6\dot{\eta})/2k$ below (see e.g. [53]).

The corresponding energy density ρ_{ax} , pressure p_{ax} , their perturbations, and the momentum density $u_{\text{ax}}\rho_{\text{ax}}$ are given by

$$\begin{aligned} \rho_{\text{ax}} &= \frac{1}{2}a^{-2}\dot{\phi}^2 + \frac{1}{2}m^2\phi^2, \\ p_{\text{ax}} &= \frac{1}{2}a^{-2}\dot{\phi}^2 - \frac{1}{2}m^2\phi^2, \\ \delta\rho_{\text{ax}} &= a^{-2}\dot{\phi}\delta\dot{\phi} + m^2\phi\delta\phi, \\ \delta p_{\text{ax}} &= a^{-2}\dot{\phi}\delta\dot{\phi} - m^2\phi\delta\phi, \\ u_{\text{ax}}\rho_{\text{ax}} &= a^{-2}k\dot{\phi}\delta\phi, \end{aligned} \quad (3)$$

and influence cosmological observables through their gravitational effects. Once $m \gg H$, these quantities also exhibit rapid oscillations, making the joint system of linear perturbation equations difficult to solve directly.

To complete the ULA system, we also require initial conditions for the ULA field. In the limit $a \rightarrow 0$, i.e. $m/H \rightarrow 0$, the field is frozen. Only its initial background value ϕ_{ini} is finite, and all other field quantities approach zero for adiabatic fluctuations. Numerically, however, one evolves from a finite initial time and at that time the field has a finite time derivative and its perturbations are generated by fluctuations in the other matter species.

We improve on current state-of-the-art ULA Boltzmann codes such as AXIONCAMB [42] by keeping the leading order term in powers of m/H as well as $k\tau$, i.e. the solution to the KG system in the radiation-dominated epoch becomes

$$\begin{aligned} \phi &\approx \phi_{\text{ini}}, & \dot{\phi} &\approx -\frac{am^2}{5H}\phi_{\text{ini}}, \\ \delta\phi &\approx \frac{m^2\dot{h}}{420aH^3}\phi_{\text{ini}}, & \dot{\delta\phi} &\approx \frac{m^2\dot{h}}{70H^2}\phi_{\text{ini}}. \end{aligned} \quad (4)$$

Thus ϕ_{ini} specifies all of the initial conditions and also determines the ULA abundance today, $\Omega_{\text{ax}} h^2$. Since $\Omega_{\text{ax}} h^2$ is an input for the code, the corresponding value of ϕ_{ini} is determined by bisecting an initial range until convergence to the desired $\Omega_{\text{ax}} h^2$ is obtained (see Appendix A for the impact of this improvement).

As an example in Fig. 1, we take a mass of 10^{-27} eV that is comparable to H at matter-radiation equality and $f_{\text{DM}} = 1$, and plot its energy density rescaled by a^3 , specifically $(\rho_{\text{ax}} h^2 / \rho_{\text{crit}})a^3$. The normalization chosen such that its final value corresponds to $\Omega_{\text{ax}} h^2 (= 0.12)$. The KG solution (thin gray curve) extends to $m/H = 100$ at the right edge of the plot. At $m \gg H$, the oscillations in the KG system become much faster $\Delta \ln a = 1$, or equivalently the dynamical time under which its gravitational effects become manifest in linear theory. The hierarchy of time scales indicates a stiff system that dramatically decreases the efficiency of numerical solvers. On the other hand, this also means that the other cosmological observables effectively only respond to the time average of the ULA oscillations, which motivates our basic approach:

1. Directly solve the KG system for $m/H < m/H_*$, where the subscript “*” labels quantities evaluated at the switch time;
2. At m/H_* , compute the effective time average (ETA) over the mass oscillation time scale;
3. Finally, evolve the time-averaged quantities for $m/H > m/H_*$ with an effective fluid approximation (EFA).

A value of $m/H_* \sim 10$, which we will see is sufficient for accuracy given current observational constraints for most masses (cf. Sec. II D), represents a switch that occurs after a few oscillations of the background density. This corresponds to the left edge of the dashed red line in Fig. 1. We next proceed to develop the steps and details of this approximation.

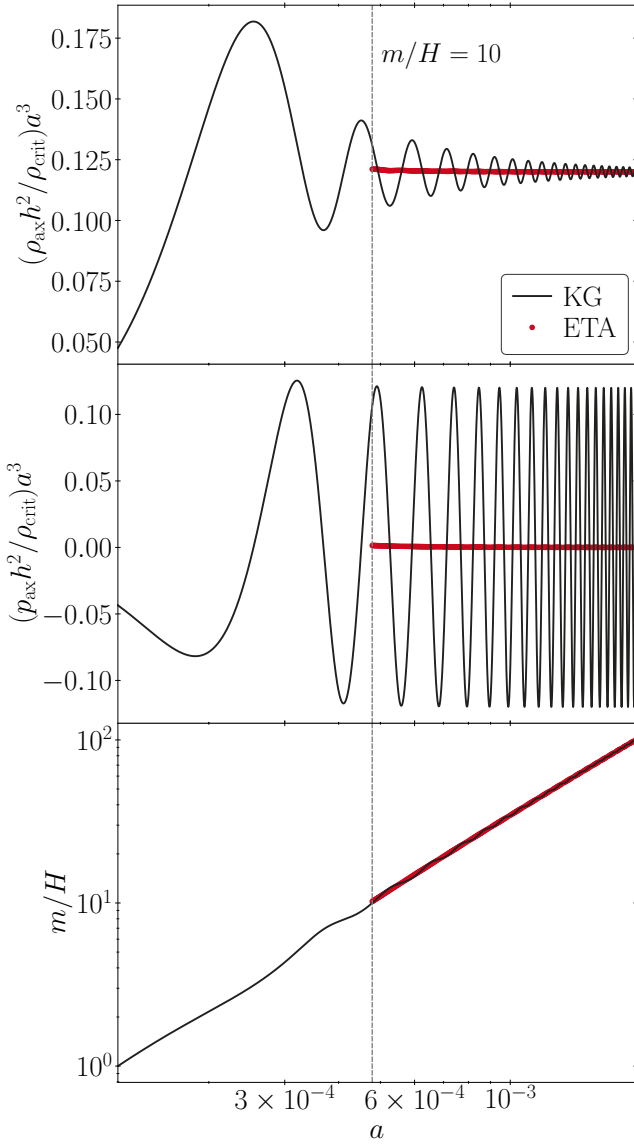


FIG. 1. Background energy density (top), pressure (middle), and m/H (bottom) for ULAs with $m = 10^{-27}$ eV and a dark matter fraction $f_{\text{DM}} = 1$. The ETA values at discrete switch times (dense red points, starting at $m/H_* = 10$) effectively average the temporal oscillations of the KG solution (solid lines). Here all ETA values take a common initial field value ϕ_{ini} determined by matching to the final density for the $m/H_* = 100$ case and the density is rescaled to reflect this present value $\rho_{\text{ax}}(a = 1)h^2/\rho_{\text{crit}} = \Omega_{\text{ax}}h^2$.

B. Effective Time Average

When the oscillations have become sufficiently rapid compared to the Hubble rate, we construct quantities that represent the effective time average, or ETA, over the oscillations, without explicitly performing a cumbersome time average for each k -mode and the background.

Our basic strategy follows Ref. [45] and technical de-

tails are provided in Appendix C. The idea developed there is to separate the sine and cosine pieces of the field oscillations at H_* for the ETA [see Eq. (B4)],

$$\begin{aligned}\phi &= \varphi_c \cos(mt - mt_*) + \varphi_s \sin(mt - mt_*), \\ \delta\phi &= \delta\varphi_c \cos(mt - mt_*) + \delta\varphi_s \sin(mt - mt_*),\end{aligned}\quad (5)$$

where we have introduced t_* , the coordinate time at H_* , for notational convenience. The two components still obey the exact KG equation and thus energy-momentum conservation, but the redundancy of describing a single field with two components means that we have the freedom to specify additional auxiliary conditions at the switch, which we take to be the same for the background and perturbations (see [45] for a detailed discussion):

$$\begin{aligned}\frac{d^2\varphi_{c,s}/dt^2}{d\varphi_{c,s}/dt} \Big|_* &= \frac{d^2\delta\varphi_{c,s}/dt^2}{d\delta\varphi_{c,s}/dt} \Big|_* \\ &= -\frac{3}{2}H^{\text{ETA}} + \frac{d\ln H^{\text{ETA}}}{dt}.\end{aligned}\quad (6)$$

These conditions are motivated by the expectation that the background fields $\varphi_{c,s} \propto a^{-3/2}$ and the perturbation fields evolve on the Hubble time with the coefficient chosen to be the same for simplicity. Note, however, that they are implicit equations since they require H^{ETA} , the ETA of H , which must itself be obtained from constructing $\rho_{\text{ax}}^{\text{ETA}}$.

Apart from this subtlety, which we address below, $\rho_{\text{ax}}^{\text{ETA}}$ and the other corresponding ETA variables are defined from $\varphi_{c,s}$ through Eq. (3) using the usual cycle-average replacement rules for sinusoidal functions ($\cos^2 = \sin^2 \rightarrow 1/2$ and $\cos \cdot \sin \rightarrow 0$) [45]: for example,

$$\begin{aligned}\rho_{\text{ax}}^{\text{ETA}} &= \frac{1}{2}m^2(\varphi_c^2 + \varphi_s^2) + \frac{1}{4a^2}(\dot{\varphi}_c^2 + \dot{\varphi}_s^2) \\ &\quad + \frac{m}{2a}(\varphi_s \dot{\varphi}_c - \varphi_c \dot{\varphi}_s)\end{aligned}\quad (7)$$

and likewise for (see Eq. C8)

$$\{p_{\text{ax}}^{\text{ETA}}, \delta\rho_{\text{ax}}^{\text{ETA}}, \delta p_{\text{ax}}^{\text{ETA}}\}, \quad (8)$$

whereas the same procedure for $(u_{\text{ax}}\rho_{\text{ax}})^{\text{ETA}}$ defines

$$u_{\text{ax}}^{\text{ETA}} \equiv \frac{(u_{\text{ax}}\rho_{\text{ax}})^{\text{ETA}}}{\rho_{\text{ax}}^{\text{ETA}}} \equiv \frac{(u\rho)^{\text{ETA}}}{\rho_{\text{ax}}^{\text{ETA}}}. \quad (9)$$

The ETA of the Hubble parameter then becomes

$$(H^{\text{ETA}})^2 = -\frac{K}{a^2} + \frac{8\pi G}{3} \sum_{i \neq \text{ax}} \rho_i + \rho_{\text{ax}}^{\text{ETA}}, \quad (10)$$

where $K = -\Omega_K H_0^2$ is the background curvature parameter. Here and below, we use the shorthand notation $(\dots)^{\text{ETA}}$ to refer to ETA evaluation of the ULA quantities.

To address the implicitness of Eq. (6), we iterate the construction of $\varphi_{c,s}$ and H^{ETA} from a starting guess of

$H = H^{\text{ETA}}$ until convergence in Eq. (6) and Eq. (10) is achieved (see Appendix C for details). This iteration, new to our approach, is not a significant correction for the case when the ULAs are themselves gravitationally insignificant compared with other matter components at the switch [45] but always removes the leading order oscillation in H regardless.

We show the resulting evolution of $\rho_{\text{ax}}^{\text{ETA}}$ and H^{ETA} in Fig. 1. In this section alone, we take the ETA at multiple but discrete switch times (red dots) to illustrate the dependence on m/H_* . Consequently the initial field value ϕ_{ini} is also taken to be the same for all m/H_* switch values and defined so that $m/H_* = 100$ gives the correct final density $\Omega_{\text{ax}} h^2$. In the final AxECAMB method, there is only a single m/H_* corresponding to the switch to EFA and ϕ_{ini} is defined by its value.

The advantage of this algorithm is that H^{ETA} always gives the effective time-averaged expansion rate regardless of the particular phase at which the switch catches the KG oscillations (see Fig. 1). The design of this procedure introduces a discontinuity between H and H^{ETA} at the switch to EFA. Other approaches demand continuity in ρ_{ax} between KG and EFA and therefore H but notice that no condition can provide continuity in both ρ_{ax} and p_{ax} simultaneously. Pressure discontinuities cause spurious Jeans oscillations in the perturbations as we discuss in Appendix D. Our approach also avoids the problem that the oscillations relative to ETA in ρ_{ax} only decay as $\mathcal{O}(H/m)$, which would cause relatively large errors in the continuous ρ_{ax} approach.

We proceed to define the ETA of metric perturbations in the same way. The metric perturbations themselves are determined from the matter perturbations via the perturbed Einstein equations; in particular, the time-time (00), time-space (0*i*), and their combination with the trace-free space-space (*ij*) Einstein equations are

$$\begin{aligned} \frac{1}{2} \frac{\dot{a}}{a} \dot{h} - (k^2 - 3K)\eta &= 4\pi G a^2 \sum_i \delta\rho_i, \\ \dot{\eta} - \frac{K}{k}\sigma &= 4\pi G a^2 \sum_i u_i \rho_i / k, \\ \dot{\sigma} + \frac{\dot{a}}{a}\sigma &= -4\pi G a^2 \sum_i \left[2\frac{p_i \pi_i}{k} \right. \\ &\quad \left. + \frac{\delta\rho_i + 3(\dot{a}/a)\rho_i u_i / k}{k - 3K/k} \right], \end{aligned} \quad (11)$$

where $p_i \pi_i$ is the anisotropic stress fluctuation of each component, with $\pi_{\text{ax}} = 0$. Like the background equation for H , these equations transfer the oscillations in $\rho_{\text{ax}}, \delta\rho_{\text{ax}}, u_{\text{ax}}$ to the metric fluctuations. Unlike the background equations, these are differential equations, hence those impacts on the metric fluctuations are not solely determined by the KG field variables at the switch, and again require auxiliary conditions to determine fully.

The auxiliary conditions for the metric fluctuations should uniquely specify the ETA of two independent linear combinations of metric fluctuations, which we can

choose without loss of generality to be η and σ . One algebraic combination from the ETA of the matter sources comes from the 00 and 0*i* equations:

$$\left(\frac{aH}{k} \sigma - \eta \right)^{\text{ETA}} = \left(4\pi G a^2 \sum_i \frac{\delta\rho_i + 3\rho_i u_i aH/k}{k^2 - 3K} \right)^{\text{ETA}}, \quad (12)$$

leaving the freedom to define the partitioning of the ETA of the matter sources between η^{ETA} and σ^{ETA} . This choice must obey causality, namely the conservation of curvature for super-horizon adiabatic modes. Given the 0*i* equation, the deviation induced by free-fall velocities represented by $u_i = \mathcal{O}(k/aH)^3$ (see e.g. [54]) requires that η is conserved with only $\mathcal{O}(k/aH)^2$ corrections and hence does not respond to the ULA oscillations. Thus,

$$\eta^{\text{ETA}} \approx \eta \quad (k/aH \ll 1), \quad (13)$$

and σ^{ETA} follows from Eq. (12).

Conversely, for $k/aH \gg 1$ where η evolves with u_{ax} given the 0*i* equation, the 00 equation implies that η will directly reflect the ULA oscillations from $\delta\rho_{\text{ax}}$ and evolve $\propto (H/m)$, whereas the *ij* equation implies that σ will reflect the time integral of these ULA oscillations, and so be suppressed by an additional H/m factor to be $\propto (H/m)^2$ even without ETA. Thus, to remove the leading order oscillations, we take

$$\sigma^{\text{ETA}} \approx \sigma \quad (k/aH \gg 1), \quad (14)$$

and η^{ETA} can be obtained in turn from Eq. (12) to remove the $\mathcal{O}(H/m)$ oscillations in η .

Thus, σ and η oscillate in different regimes, motivating an empirical weight to mediate the transition and fully specify the ETA partitioning

$$\frac{\Delta\eta}{\Delta\sigma} \equiv \frac{\eta - \eta^{\text{ETA}}}{\sigma - \sigma^{\text{ETA}}} = -\frac{aH^{\text{ETA}}}{k} \frac{W}{1-W}, \quad (15)$$

where the weight

$$W = \frac{(k/aH^{\text{ETA}})^2}{3 + (k/aH^{\text{ETA}})^2}. \quad (16)$$

Here the use of H^{ETA} rather than H prevents the weight from being sensitive to the phase of the KG oscillation. The scaling is motivated by the arguments above and the constant 3 is chosen to roughly optimize the error in evaluating the CMB power spectra and total transfer function, although the error is in fact not very sensitive to the precise value. Nonetheless, this empirical scaling produces excellent agreement with numerical results for the amplitude of the metric oscillations as shown in Appendix C.

Finally, with the partitioning of Eq. (16), the KG values of σ and η at the switch, and Eq. (12) for the matter ETA source, we solve for σ^{ETA} and η^{ETA} . In Fig. 2, we illustrate this construction for a super-horizon mode $k = 10^{-4} \text{ Mpc}^{-1}$ and a sub-horizon mode $k = 0.055 \text{ Mpc}^{-1}$,

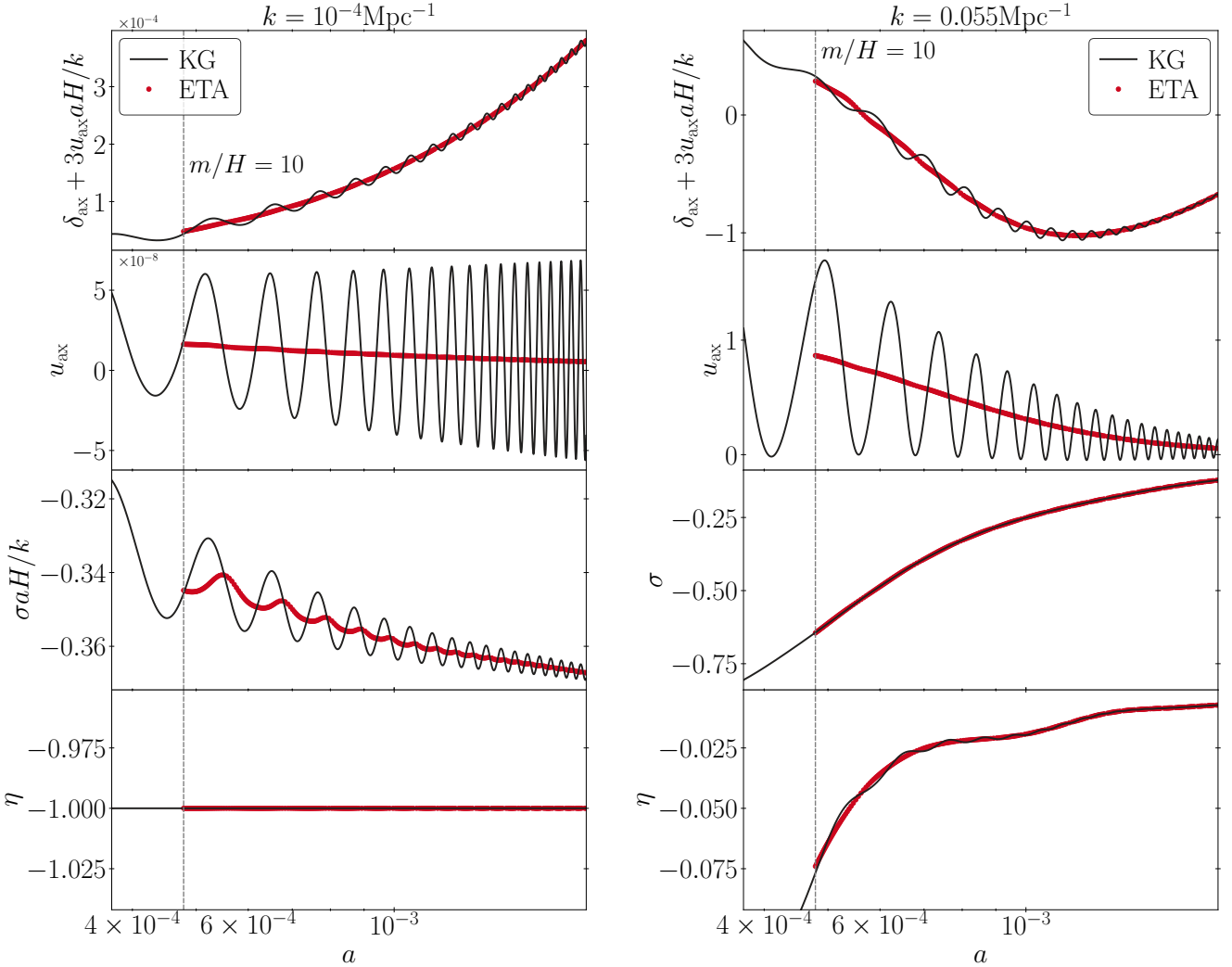


FIG. 2. Metric and ULA perturbations (solid lines) and their ETA values (red points) with the same model as Fig. 1 ($m = 10^{-27}$ eV, $f_{\text{DM}} = 1$) for a superhorizon mode $k = 10^{-4}$ Mpc $^{-1}$ (left) and a subhorizon mode $k = 0.055$ Mpc $^{-1}$ (right). The temporal range spans $m/H = 7 \sim 100$, with the start of the ETA at $m/H = 10$ marked with the vertical dashed line. In each case the ETA effectively time averages the leading order KG oscillation (see text for discussion).

corresponding to the two limiting behaviors of Eqs. (13) and (14). In the top panels for both modes, we plot the ULA variables $\delta_{\text{ax}} + 3u_{\text{ax}}aH/k$ and u_{ax} , with m/H varying from 7 to 100 across the plot and ETA starting at $m/H = 10$. This verifies that the ETA does effectively average over the temporal oscillations of the KG system and removes the leading order terms in H/m . Note that $u_{\text{ax}}^{\text{ETA}}$ approaches zero as H/m decreases whereas the KG oscillations are unsuppressed by powers of H/m which we will see makes the former a much better match to the EFA. On the metric side, for the superhorizon mode, η remains constant as expected from Eq. (13) and its ETA is accordingly the same value. As dictated by Eq. (12), the KG oscillations in the ULA are then transferred to σ through $\sigma aH/k$, and its ETA does remove the KG oscillations to leading order in H/m , albeit with a noticeable

$(H/m)^2$ fractional residual which improves rapidly for later switches.

In the subhorizon panel, we plot σ rather than $\sigma aH/k$ and verify the expectations of Eq. (14) that σ in the KG system does not oscillate at $\mathcal{O}(H/m)$. Instead, η carries these oscillations of the KG system and the ETA effectively removes this leading order term. While $\sigma aH/k$ would still oscillate, its oscillations reflect those of H itself. Finally, note that at late times but before the ULAs fall into baryonic potential wells, the velocity $v_{\text{ax}}^{\text{ETA}} \equiv u_{\text{ax}}^{\text{ETA}}/(1+w_{\text{ax}}^{\text{ETA}}) \approx u_{\text{ax}}^{\text{ETA}} \rightarrow -\sigma$, which is the expectation from hydrostatic equilibrium where Newtonian gauge velocities are driven to zero (Appendix D).

In summary, for all matter and metric variables and scales, the ETA procedure effectively removes the KG oscillations at the $\mathcal{O}(H/m)$ level and attains at least

$\mathcal{O}(H/m)^2$ accuracy. The ETA procedure then removes the sensitivity to the phase of the KG oscillations at the chosen switch time to this order. In principle, this procedure could be refined to capture the next order, but as we shall see in Sec. II D, the accuracy of cosmological observables is already sufficiently high for $m \gg 10H_{\text{eq}}$ or for $f_{\text{DM}} \ll 1$, and when higher accuracy is required, it is easier to simply raise the value of m/H_* accordingly.

C. Effective Fluid Approximation

We have shown that the ETA gives us an accurate prescription of the time-average of the KG variables at any desired value of the switch time and is robust to the phase of the KG oscillations at leading order in H/m , unlike other techniques. From that switch time, we can then evolve the time average under an effective fluid approximation, i.e. EFA, provided that we can accurately characterize the latter using a fluid description and conservation of energy-momentum.

By implementing this as a code switch in AxieCAMB, no evolution variables are solved across the discontinuity introduced by the switch (see Appendix E). Instead, the ETA provides the initial or switch conditions for the separate evolution of the EFA. Unlike in the tests of the previous section, there is no need to solve the KG system past the switch. Therefore, in this section, we compare the EFA evolved system from a fiducial switch time $m/H_* = 10$ to the ETA evolution established previously, and assess the errors induced by the switch conditions and the EFA modeling.

To model the EFA, we first need to characterize the effective fluid equation of state $w_{\text{ax}}^{\text{EFA}}$. Following Ref. [45], we parameterize the time evolution of $w_{\text{ax}}^{\text{EFA}}$ as

$$w_{\text{ax}}^{\text{EFA}} \equiv \frac{p_{\text{ax}}^{\text{EFA}}}{\rho_{\text{ax}}^{\text{EFA}}} = A_w \left(\frac{H}{m} \right)^2, \quad (17)$$

where A_w is a constant to be specified, and the scaling with H is motivated by the behavior of $p^{\text{ETA}}/\rho^{\text{ETA}}$ (see Appendix E and Fig. 25). This equation of state defines the evolution of the background via the continuity equation

$$\dot{\rho}_{\text{ax}}^{\text{EFA}} + 3(1 + w_{\text{ax}}^{\text{EFA}}) \frac{\dot{a}}{a} \rho_{\text{ax}}^{\text{EFA}} = 0, \quad (18)$$

as well as the adiabatic sound speed

$$c_{\text{ad}}^2 \equiv \frac{\dot{p}_{\text{ax}}^{\text{EFA}}}{\dot{\rho}_{\text{ax}}^{\text{EFA}}} = w_{\text{ax}}^{\text{EFA}} \left(\frac{1 + w_T}{1 + w_{\text{ax}}^{\text{EFA}}} + 1 \right), \quad (19)$$

where $w_T = p_T/\rho_T$ is the total equation of state. With the effective method for the background complete, we find the initial field ϕ_{ini} that corresponds to the final $\Omega_{\text{ax}} h^2$ by bisecting initial field values until sufficient convergence is achieved. A final subtlety applies to the definition of $\Omega_{\text{ax}} h^2$ itself. For masses $m \geq 10H_0$, we

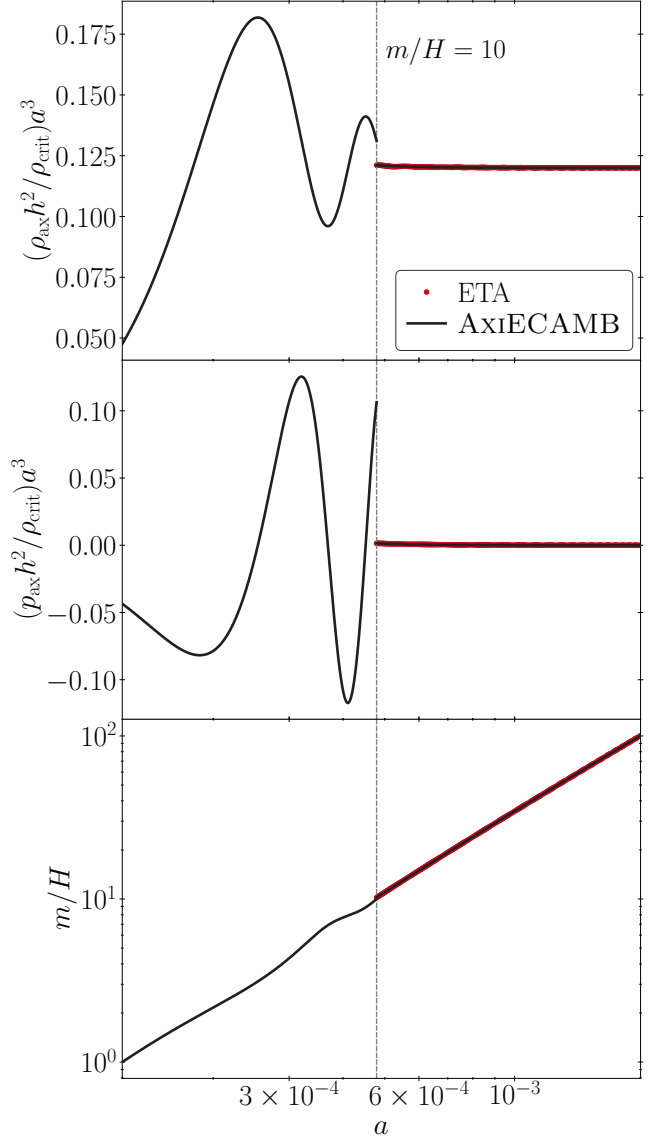


FIG. 3. Background evolution of the full AxieCAMB method from KG to EFA (solid lines, with the switch to EFA at $m/H_* = 10$) compared with ETA (red points after $m/H = 10$) for the same case as Fig. 1 ($m = 10^{-27}$ eV, $f_{\text{DM}} = 1$).

use $\rho_{\text{ax}}^{\text{ETA}}(a = 1)$ and $H_0 = H^{\text{ETA}}(a = 1)$ even when m/H_* is at $a > 1$, since cosmological observables reflect the Hubble time averaged effect of ULAs.³ For masses where $m/H_0 < 10$, the oscillations are not rapid at the present and we use the instantaneous $\rho_{\text{ax}}(a = 1)$ and $H_0 = H(a = 1)$ solved from the KG system. In this latter regime, the ULA behave as dark energy all the way to the present.

³ Technically this is achieved by forcing a switch at $a = 1 - 10^{-3}$ and using $\rho_{\text{ax}}^{\text{EFA}}$ at $a = 1$.

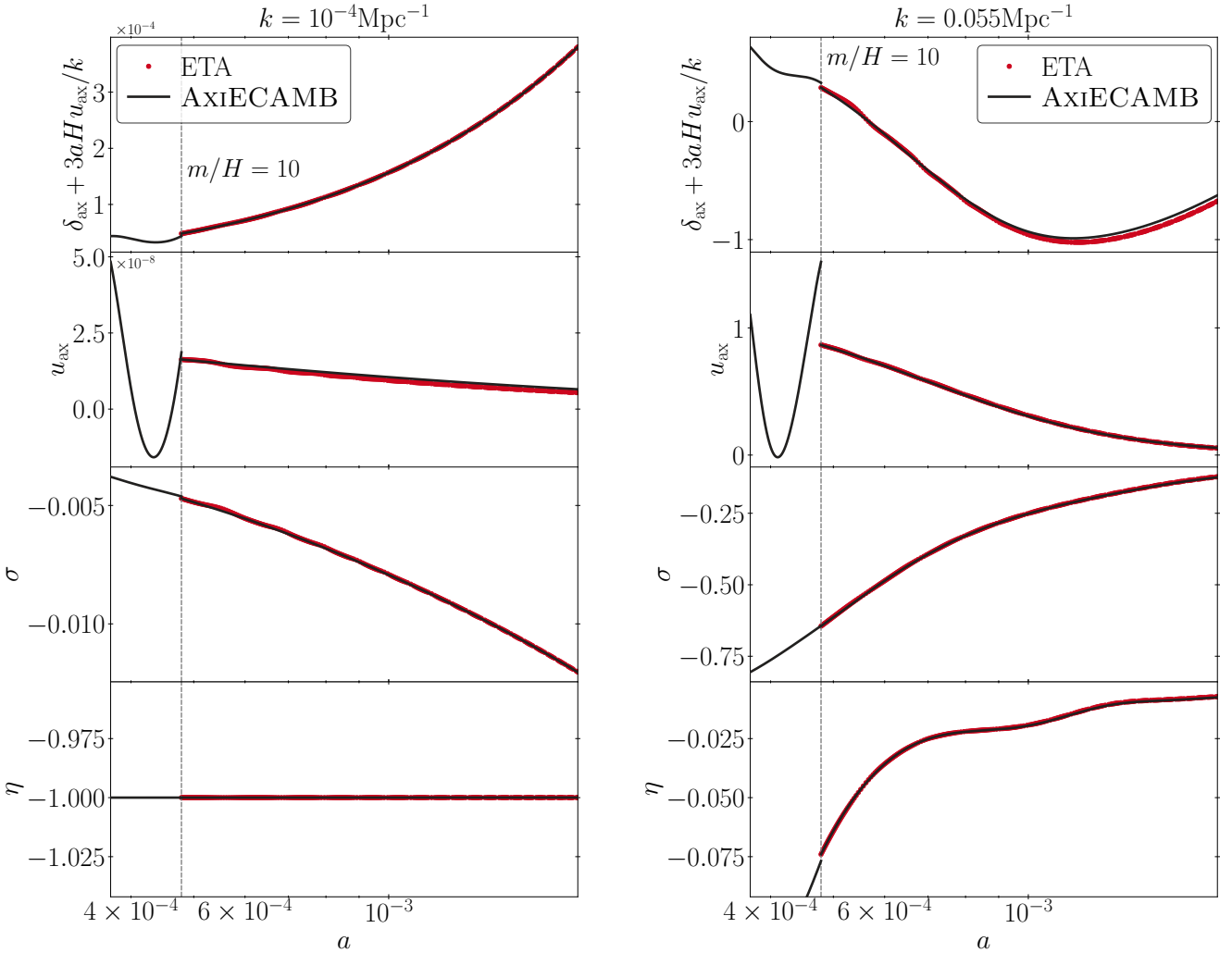


FIG. 4. Perturbation evolution of the AxIECAMB method (solid line) compared with ETA (red points) for the same modes as Fig. 2. The switch occurs at $m/H_* = 10$ and the temporal range extends to $m/H = 100$.

Proceeding to the perturbations, we define the fluid pressure perturbation by the rest frame sound speed [55], which we take as

$$c_{\text{ax}}^2 = \left[\frac{\sqrt{1 + (\frac{k}{am})^2} - 1}{\frac{k}{am}} \right]^2 + A_c \left(\frac{H}{m} \right)^2, \quad (20)$$

where A_c is a constant to be specified at the switch by the pressure perturbation as $k \rightarrow 0$ where the first term vanishes. This form is also motivated by the ETA of KG oscillations $\delta p_{\text{ax}}^{\text{ETA}} / \delta \rho_{\text{ax}}^{\text{ETA}}$ (see Appendix B). Energy-momentum conservation dictates that the perturbation fluid variables obey

$$\begin{aligned} \dot{\delta \rho}_{\text{ax}}^{\text{EFA}} + 3 \frac{\dot{a}}{a} (\delta \rho + \delta p)_{\text{ax}}^{\text{EFA}} &= -k(\rho u)_{\text{ax}}^{\text{EFA}} - (\rho + p)_{\text{ax}}^{\text{EFA}} \frac{\dot{h}}{2}, \\ \left[\frac{d}{d\tau} + 4 \frac{\dot{a}}{a} \right] (\rho u)_{\text{ax}}^{\text{EFA}} &= k \delta p_{\text{ax}}^{\text{EFA}}, \end{aligned} \quad (21)$$

where

$$\delta p_{\text{ax}}^{\text{EFA}} = c_{\text{ax}}^2 \delta \rho_{\text{ax}}^{\text{EFA}} + 3 (c_{\text{ax}}^2 - c_{\text{ad}}^2) \frac{aH}{k} (\rho u)_{\text{ax}}^{\text{EFA}}. \quad (22)$$

In the code itself, we evolve $\delta \rho_{\text{ax}}^{\text{EFA}} \equiv \delta \rho_{\text{ax}}^{\text{EFA}} / \rho_{\text{ax}}^{\text{EFA}}$ and the momentum flux $u_{\text{ax}}^{\text{EFA}} \equiv (\rho u)_{\text{ax}}^{\text{EFA}} / \rho_{\text{ax}}^{\text{EFA}}$.

To fully determine the EFA solutions, we need the switch values of the matter and metric variables as well as the constants A_w and A_c which define the equation of state and sound speed after the switch. Errors from both contribute to the final error of our approach. The original approach in Ref. [45] was to derive $A_w = 3/2$ analytically in radiation domination (i.e. appropriate for $m \gg 10H_{\text{eq}}$) to minimize equation of state errors, and to fix $A_c = 5/4$ by setting $\lim_{k \rightarrow 0} c_{\text{ax}}^{\text{EFA}} = c_{\text{ax}}^{\text{ETA}}$ to minimize switching errors instead (see Appendix B). This method has the disadvantage that $p_{\text{ax}}^{\text{EFA}}$ and $v_{\text{ax}}^{\text{EFA}}$ are discontinuous with their ETA equivalents, which both induces discontinuities in the metric and other observables if $m \lesssim 10H_{\text{eq}}$, and

breaks hydrostatic equilibrium below the Jeans scale (see Appendix D). Furthermore, their procedure would give a result that differs from $A_w = 3/2$ when the background is not radiation dominated, removing the advantage of having an analytic prescription.

With these considerations, we modify the approach of Ref. [45] to make the EFA to ETA pressure continuous by instead deriving A_w from its ETA value at the switch. This gives our final choice for the switch conditions to the EFA at m/H_* :

$$(p, \rho, \delta\rho, u)_{\text{ax}}^{\text{EFA}} = (p, \rho, \delta\rho, u)_{\text{ax}}^{\text{ETA}}, \quad (23)$$

which then automatically sets

$$(H, \sigma, \eta)^{\text{EFA}} = (H, \sigma, \eta)^{\text{ETA}} \quad (24)$$

as well as the value of

$$A_w = \frac{p_{\text{ax}}^{\text{ETA}}}{\rho_{\text{ax}}^{\text{ETA}}} \left(\frac{m}{H_*^{\text{ETA}}} \right)^2, \quad (25)$$

since $w_{\text{ax}}^{\text{EFA}} = w_{\text{ax}}^{\text{ETA}}$. For simplicity, we keep $A_c = 5/4$ since the impact of a refined treatment is minimal in practice (see Appendix B for the comparison to analytic expectations).

For the background, this completes the AxECAMB method. In Fig. 3 we compare the background evolution obtained using this approach for a switch at $m/H_* = 10$ with the ETA after the switch, using the same mass (10^{-27} eV) and ULA fraction in dark matter ($f_{\text{DM}} = 1$) as in Fig. 1. In the EFA regime fractional differences are nearly invisible and substantially below $(H_*/m)^2 = 0.01$.

The same comparison is carried out for the perturbation variables in Fig. 4 after the fiducial switch $m/H_* = 10$ for the same k -modes as in Fig. 2. For the superhorizon mode (left panels), small differences in u_{ax} come mostly from the modeling of the EFA sound speed c_{ax}^2 but the overall impact on the dynamically relevant density perturbation is negligible. On these scales, the synchronous gauge v_{ax} reflects tiny deviations from free-fall, where $v_{\text{ax}} = 0$, due to the finite pressure perturbation as $k \rightarrow 0$. For σ , the main error initially is the matching error due to the visible oscillations in ETA at $\mathcal{O}(H/m)^2$ which do not track the mean of the KG system. Since σ is dynamically sourced by density fluctuations according to Eq. (11), this main error evolves away. The curvature η remains properly conserved under both ETA and EFA.

For the subhorizon mode, there are also matching and evolution errors. In the density and momentum perturbations there are small oscillations in the ETA that are again carried forward by the EFA. The fractional errors in the density perturbation are in the regime where the perturbation itself is already highly suppressed (see Fig. 8). Notably, η shows only $\mathcal{O}(H/m)^2$ differences but carries oscillations on a longer time scale. These are associated with the acoustic oscillations of the photon-baryon system. While the errors that are transferred via the metric remain $(8\pi G \rho_{\text{ax}}/3H^2)\mathcal{O}(H^2/m^2)$, a later switch time

than $m/H_* = 10$ is required to achieve better than percent level accuracy for large f_{DM} , which we will address in detail in the next section.

D. Switch time and CMB sources

One major goal of our code AxECAMB is accurate predictions of CMB observables for all ULA masses. This places additional requirements on the switch time m/H_* when it is near matter-radiation equality or recombination. In addition, the discontinuities at the switch require that CMB anisotropy source functions be augmented with boundary terms.

The first consideration pertains to cases where the switch is near matter-radiation equality and $f_{\text{DM}} \sim 1$, which, as we noted in the previous section, needs an $m/H_* > 10$ switch to ensure better than 1% accuracy in the metric and thus also for the CMB. We expect that at $(8\pi G \rho_{\text{ax}}/3H^2)\mathcal{O}(H^2/m^2)$, photons respond to the KG oscillations through the metric perturbations as shown in Appendix E. The proportionality factor in this scaling can also be k -dependent since for $k/aH \gg 1$, the acoustic frequency is larger than the Hubble rate.

While our ETA procedure in Eq. (12) removes the leading order effects from the KG oscillations, it does not address these higher-order responses. Furthermore, the strong sensitivity of CMB anisotropy to the epoch of recombination means that it is always better to avoid placing the switch there regardless of f_{DM} .

Specifically, starting from a baseline switch choice of $m/H_* (= 10$ for our default accuracy), we raise the m/H_* value of the switch in two ways:

- For $m < 10^{-25}$ eV, if the baseline switch is after $\rho_{\text{ax}}/\rho_r = 0.03$ (estimated by assuming the ULA redshift as matter after the switch), but before $z = 1300$, increase m/H_* to around twice the baseline value, specifically corresponding to the best mass-oscillation phase (see below).
- Then, if the proposed switch is near recombination $z_* \in (800, 1300]$, increase m/H_* such that the switch is just below $z = 800$.

In the first step, we have taken advantage of the independence of our ETA technique on the phase of the KG oscillations to further improve accuracy over the naive scaling by choosing the phase that minimizes the response in the photon-baryon acoustic oscillations to the switch phase (see Appendix E for details). In the second step, we reduce switch artefacts in the CMB anisotropy source function itself by not allowing the switch to occur near recombination, where it would otherwise be by default for $m \sim 10^{-27.5}$ eV (see Fig. 28). We discuss this source function next. The combination of these steps affects masses $10^{-27.5} \lesssim m/\text{eV} \lesssim 10^{-25}$. In this regime, the first step only applies to cases where $f_{\text{DM}} \gtrsim (m/10^{-23.5}\text{eV})^{1/2}$.

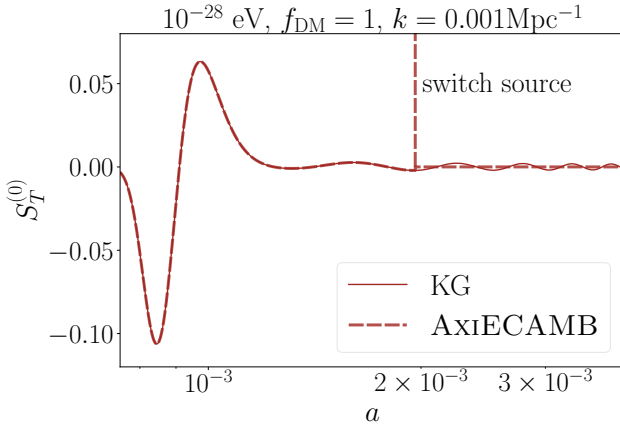


FIG. 5. Total CMB source function $S_T^{(0)}$ in Eq. (31) for $m = 10^{-28}$ eV, $f_{\text{DM}} = 1$, $k = 0.001 \text{Mpc}^{-1}$. The thin solid black line is the KG solution and the thick red dashed line is our effective theory for a switch at $m/H_* = 10$. At the switch, the integration by parts adds a boundary term or delta function source represented here by the vertical line.

With this procedure for setting the switch time m/H_* , the methodology of the matter and metric evolution for AxECAMB is complete. On the other hand, CMB Boltzmann codes obtain their anisotropy predictions by a line-of-sight integral of the perturbation sources. For example, the CMB temperature power spectrum is given by (see e.g. Ref. [56])

$$C_\ell^{TT} = 4\pi \int d\ln k \Delta_\ell^{T(0)} \Delta_\ell^{T(0)} \mathcal{P}_R(k), \quad (26)$$

where $\mathcal{P}_R(k)$ is the initial curvature power spectrum, and the photon transfer function $\Delta_\ell^{T(0)}$ is the integral over the $S_{T_j}^{(0)}$ source functions

$$\begin{aligned} \Delta_\ell^{T(0)} &= \int d\tau \sum_{j=0}^2 S_{T_j}^{(0)} \phi_\ell^{j0} [\chi, \nu] \\ &\equiv \int d\tau S_T^{(0)} \phi_\ell^{00} [\chi, \nu] + B_\ell^{T(0)}. \end{aligned} \quad (27)$$

Here ϕ_ℓ^{jm} are the radial eigenfunctions for an jm multipole source and are given explicitly by the hyperspherical Bessel functions [57] while the radial distance of the source $\chi = \sqrt{|K|} \cdot (\tau_0 - \tau)$ and wavenumber $\nu = \sqrt{k^2 + K}/\sqrt{|K|}$ are given in terms of the FRW spatial curvature K and $\tau_0 = \tau(a = 1)$. The S_{T_j} source functions are given by

$$S_{T_0}^{(0)} = e^{-\mu} \left(\frac{\dot{\mu}\delta_\gamma}{4} - \frac{\dot{h}}{6} \right), \quad (28)$$

$$S_{T_1}^{(0)} = e^{-\mu} \dot{\mu} v_b, \quad (29)$$

$$S_{T_2}^{(0)} = e^{-\mu} \left(\dot{\mu} P^{(0)} + \frac{2}{3} \sqrt{k^2 - 3K} \sigma \right), \quad (30)$$

where δ_γ is the photon density perturbation, $\dot{\mu} = n_e \sigma_T a$ is the Thomson opacity, v_b is the baryon velocity, and $P^{(0)}$ is the photon polarization source [57]. Note that the total source function $S_T^{(0)}$ is then defined via integration by parts using relationships between the hyperspherical Bessel functions,

$$S_T^{(0)} = S_{T_0}^{(0)} + \frac{\dot{S}_{T_1}^{(0)}}{k} + \frac{1}{2} \frac{k^2 S_{T_2}^{(0)} + 3\ddot{S}_{T_2}^{(0)}}{k\sqrt{k^2 - 3K}}, \quad (31)$$

and $B_\ell^{T(0)}$ is the boundary term associated with the integration by parts.⁴ Usually the boundary term vanishes since the boundaries are at $\tau = 0$ and $\tau = \tau_0$ but for our case where there is a new boundary at the switch which implies

$$B_\ell^{T(0)} = \frac{3 \left(\Delta S_{T_2}^{(0)} \dot{\phi}_\ell^{00} - \Delta \dot{S}_{T_2}^{(0)} \phi_\ell^{00} \right)}{2k\sqrt{k^2 - 3K}} - \frac{\Delta S_{T_1}^{(0)} \phi_\ell^{00}}{k}, \quad (32)$$

evaluated at τ_* where the boundary change Δ of any quantity X is defined as

$$\Delta X = X^{\text{KG}} - X^{\text{EFA}} \quad (33)$$

and similarly for the derivative. More explicitly, given our KG to EFA transition the nonvanishing switch source contributions are⁵

$$\begin{aligned} \frac{\Delta S_{T_2}^{(0)}}{\sqrt{k^2 - 3K}} &= \frac{2}{3} e^{-\mu} \Delta \sigma, \\ \frac{\Delta \dot{S}_{T_2}^{(0)}}{\sqrt{k^2 - 3K}} &= \frac{2}{3} e^{-\mu} \left[k \Delta \eta + \frac{11}{10} \dot{\mu} \Delta \sigma - 2a \Delta(H\sigma) \right], \end{aligned} \quad (34)$$

where we have used Eq. (11) and Ref. [57] (their Eqs. 38,42) to obtain

$$\begin{aligned} \Delta \dot{\sigma} &= k \Delta \eta - 2a \Delta(H\sigma), \\ \frac{\Delta \dot{P}^{(0)}}{\sqrt{k^2 - 3K}} &= \frac{1}{15} \Delta \sigma. \end{aligned} \quad (35)$$

Fig. 5 shows the total source function $S_T^{(0)}$ for $m = 10^{-28}$ eV and $k = 10^{-3} \text{Mpc}^{-1}$ with a switch after recombination. In Λ CDM, the source function after recombination gives the integrated Sachs-Wolfe effect which is negligible for this super-horizon mode at the switch

⁴ Integration by parts is employed in codes based on CMBFAST [58] such as CAMB [<http://camb.info>] where only the hyperspherical Bessel function itself is constructed, but not in CLASS [59], where the multipole sources are directly integrated using the radial functions.

⁵ Technically, the derivatives of $\dot{\mu}$ carry the difference in the expansion rate (ΔH) but its values are interpolated across the switch and the derivative of the interpolation function is continuous. This also makes the procedure transparent to improvements in the treatment of recombination.

epoch. With ULA dark matter it is suppressed by $(m/H)^2$ in the KG system as well. Notice however that because the quadrupole source $S_{T_2}^{(0)}$ involves the metric fluctuation σ in Eq. (30), the integration by parts enhances these suppressed KG oscillations by a factor of m/H for each derivative in $\ddot{S}_{T_2}^{(0)}$ in Eq. (31), leading to prominent oscillations in $S_T^{(0)}$ around a nearly zero mean value. The second derivative produces an $\dot{H}\sigma$ term which then reflects the $\mathcal{O}(1)$ amplitude ULA pressure oscillations. If the KG system were solved to later times (shown to $m/H = 100$), the integration of these oscillations would have cancelling contributions but because of the switch, this cancellation is between the leading-order switch source $\Delta(H\sigma)$ and the KG integration before the switch (shown schematically as the vertical spike). The boundary terms can therefore be thought of as a delta function source (henceforth dubbed “switch source”) to the monopole and dipole sources which cancel the incomplete KG integration that is truncated at the switch. As we show in Appendix E and Fig. 29, omitting the switch sources can produce larger than cosmic variance errors at low multipoles that depend on the exact phase of the KG oscillations at the switch.

Polarization sources follow a similar form but do not require separate integration by parts and hence do not require additional boundary terms at the switch.

III. CMB AND MATTER POWER SPECTRA

We evaluate the impact of ULAs on the CMB and matter power spectra, and assess the accuracy of AxIECAMB, with the baseline switch set at $m/H_* = 10$ (see Sec. II D for details). We compare them to a high accuracy calculation which solves the exact KG system to a much later epoch of $m/H_* = 100$, a choice justified by the $\mathcal{O}(H_*/m)^2$ or smaller errors seen in Sec. II. We show the improvement of our technique over previous work through a similar comparison in Appendix A, where we also test matter power spectra fitting functions that are useful for fuzzy dark matter and more efficient than AxIECAMB for even larger masses.

In Sec. III A we first establish the target accuracy for the CMB and matter power spectra based on that of the equivalent Λ CDM computation. We then consider the accuracy of the ULA computation for cases where they comprise of all of the dark matter (Sec. III B), part of the dark matter (Sec. III C) and all of the dark energy (Sec. III D) respectively.

A. Accuracy metrics

To assess whether accuracy is sufficient for future CMB experiments, we compute the $\Delta\chi^2$ between the default

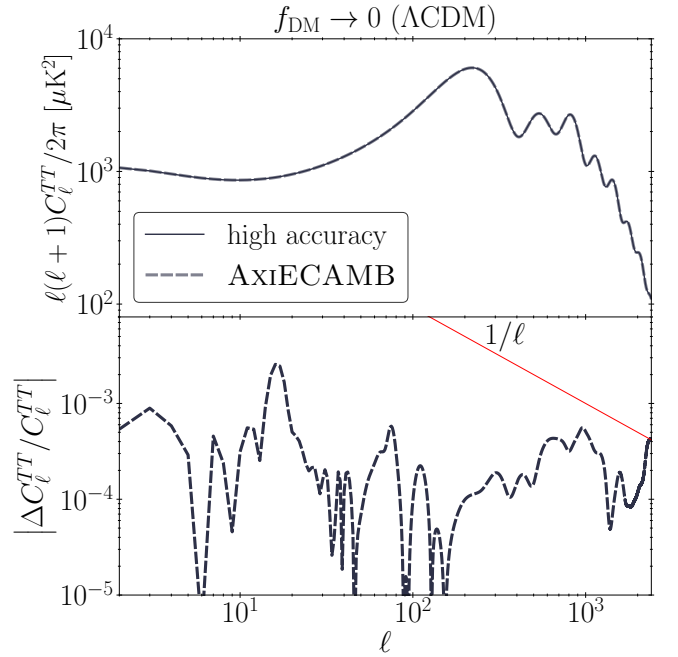


FIG. 6. Λ CDM temperature spectrum C_ℓ^{TT} (top) and its fractional error $\Delta C_\ell^{TT}/C_\ell^{TT}$ (bottom) between the default AxIECAMB and the high accuracy calculation, benchmarking the error that is not ULA related.

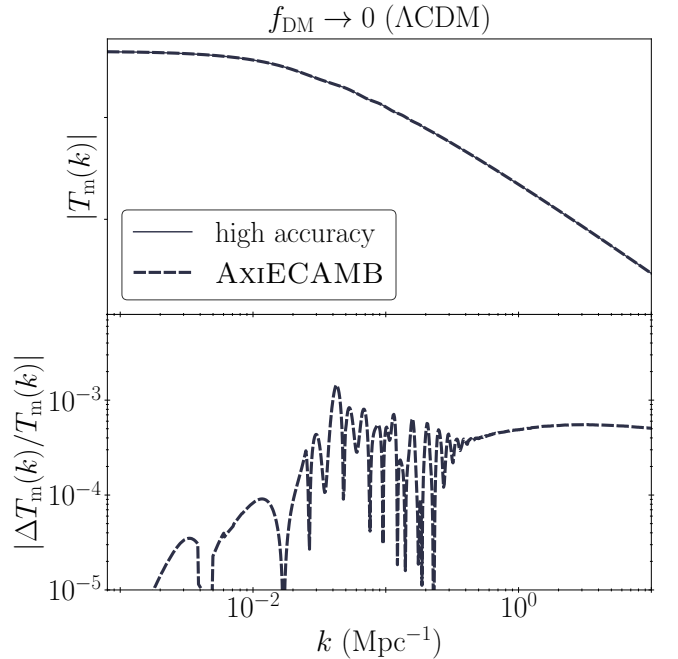


FIG. 7. Λ CDM matter transfer function $T_m(k)$ (top) and fractional error $\Delta T_m/T_m$ between the default AxIECAMB and the high accuracy calculation, benchmarking the error $\Delta T_{\text{rel}}(k)$ that is not ULA related.

and high accuracy calculations:

$$\Delta\chi^2 = \sum_{\ell=2}^{\ell_{\max}} \sum_{XY} \Delta C_\ell^X (\text{Cov}_\ell)_{XY}^{-1} \Delta C_\ell^Y, \quad (36)$$

where $X, Y \in TT, TE, EE$. The covariance matrix is between measurements of C_ℓ^X and C_ℓ^Y , which we take to be cosmic variance (CV) limited in all three spectra out to $\ell_{\max} = 2400$ (see e.g. [60]). In addition, to establish the connection between the ℓ -space errors in C_ℓ^{TT} and this type of summary statistic, we consider a cosmic variance limited experiment in TT only where

$$\Delta\chi_{TT}^2 = \sum_{\ell=2}^{\ell_{\max}} \frac{2\ell+1}{2} \left(\frac{\Delta C_\ell^{TT}}{C_\ell^{TT}} \right)^2. \quad (37)$$

Notice that the criterion that $\Delta\chi_{TT}^2 \lesssim \mathcal{O}(1)$ corresponds roughly to $|\Delta C_\ell^{TT}/C_\ell^{TT}| \lesssim 1/\ell$ for all $\ell < \ell_{\max}$ and we use this as a rough guide for cosmic variance in figures throughout.

Our choice of $\ell_{\max} = 2400$ for the CV limit corresponds roughly to the limiting accuracy of the default settings⁶ for the Λ CDM model where

$$\Delta\chi_{\Lambda\text{CDM}}^2 \approx 0.47. \quad (38)$$

In Fig. 6, we show the corresponding errors in C_ℓ^{TT} for Λ CDM. Here and below the Λ CDM case ($f_{\text{DM}} = 0$) is calculated with the same code using a finite but negligible $f_{\text{DM}} \rightarrow 0$. In the bottom panel we show that the fractional errors that contribute the most to $\Delta\chi_{TT}^2$ are at the highest ℓ where they cross $1/\ell$ line. This is mainly due to the default CMB lensing accuracy settings but note that we do not include any other secondary anisotropy sources, recombination accuracy considerations or foregrounds. Thus $\Delta\chi^2 \approx 1$ is our very conservative criteria both for negligible errors in the ULA effective method compared with the chosen cosmic variance limit and also to match the error floor set by Λ CDM.

For the matter power spectra, we treat the masses where the ULAs behave as dark matter ($m \geq 10H_0 \approx 1.44 \times 10^{-32}$ eV, $0 \leq f_{\text{DM}} \leq 1$) and dark energy ($m < 10H_0$, $0 \leq f_{\text{DE}} \leq 1$) separately in terms of whether the ULAs are included in the construction of the matter (“m”) density field along with the cold dark matter, baryons and massive neutrinos. In each regime, the impact of the ULAs is quantified by the matter transfer function relative to the high accuracy Λ CDM transfer function

$$T_{\text{rel}}(k; f_{\{\text{DM}, \text{DE}\}}) = \frac{T_{\text{m}}(k; f_{\{\text{DM}, \text{DE}\}})}{T_{\text{m}}(k; 0)}. \quad (39)$$

⁶ In terms of CAMB numerical accuracy settings, the comparison is specifically between default and high accuracy settings: `accuracy_boost = 1,6; 1_accuracy_boost = 1,8; do_late_rad_truncation = T,F; transfer_high_precision = F,T; scalcls=T,T for S8, scalcls=F,F for Tm(k)`.

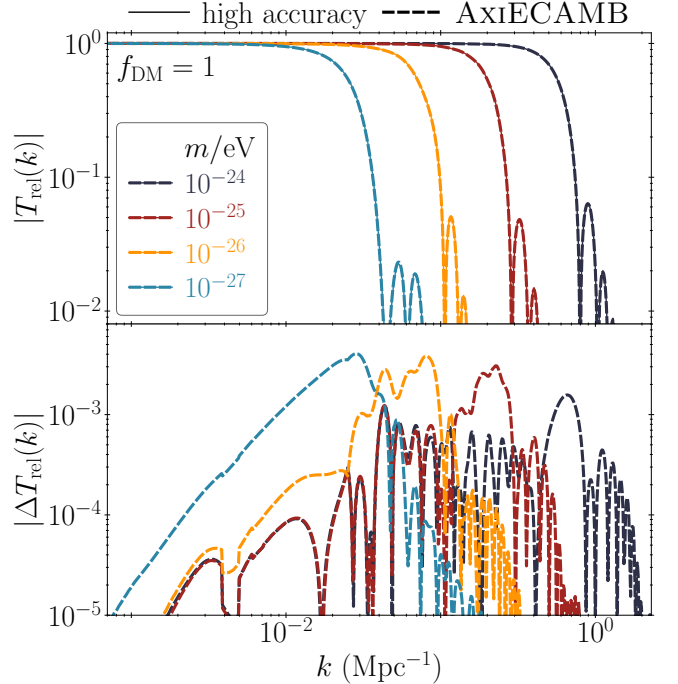


FIG. 8. Relative transfer function (top) $T_{\text{rel}}(k)$ for total DM cases ($f_{\text{DM}} = 1$) and error between the AxiECAMB and high accuracy calculations.

Note that the matter power spectrum $\mathcal{P}_{\text{m}}(k) \propto (k/H_0)^4 T_{\text{m}}^2(k) \mathcal{P}_{\mathcal{R}}(k)$.

The accuracy of the transfer function calculation in Λ CDM again sets a floor on the target accuracy of our calculations. In Fig. 7, we show these $\Delta T_{\text{m}}/T_{\text{m}}$ errors in Λ CDM. Notice that for $k \lesssim 10^{-1}$ Mpc $^{-1}$, the errors oscillate such that observable quantities that depend on the integral of the transfer function can have higher accuracy than the transfer function errors.

One such relevant quantity is $S_8 \equiv \sigma_8 \sqrt{\Omega_{\text{m}}/0.3}$ where σ_8 is the rms of the linear matter density field convolved with a spherical top-hat of radius $8h^{-1}$ Mpc. Hence we choose it as a summary statistic and use its errors in the same way as $\Delta\chi^2$ for CMB observables. Here the Λ CDM calculation places a very small floor

$$\Delta S_{8,\Lambda\text{CDM}} \approx 1.6 \times 10^{-4}, \quad (40)$$

with $S_{8,\Lambda\text{CDM}} = 0.85$. A more useful benchmark to consider is for ΔS_8 to be much better than the difference between the *Planck* Λ CDM model prediction and local measurements, e.g. $S_8 = 0.776 \pm 0.017$ with DES-Y3 [7] under Λ CDM. Under this standard, ΔS_8 should be much less than 10^{-2} .

With these benchmarks in mind, we next consider the predictions and accuracy of AxiECAMB across the range of m that spans the dark matter and dark energy regimes.

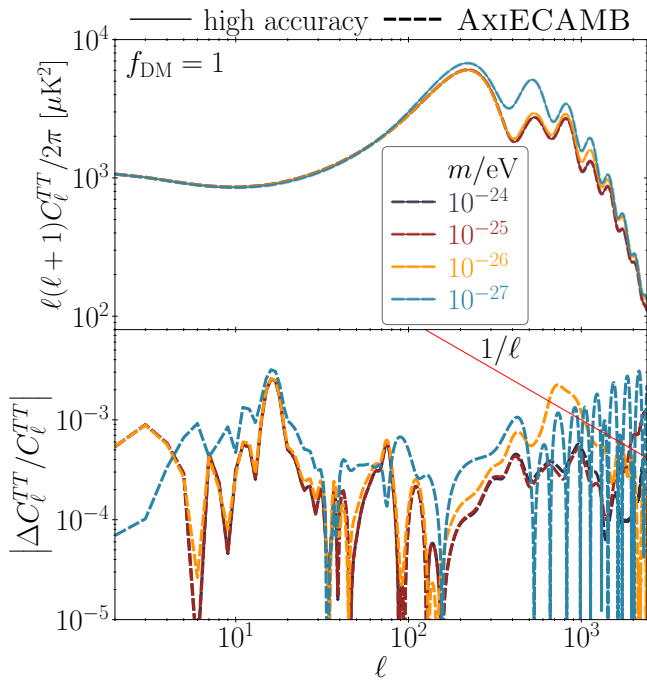


FIG. 9. C_ℓ^{TT} in the total dark matter cases (top; $f_{DM} = 1$) and its fractional error between AxIECAMB and high accuracy calculations. Red line represents the $1/\ell$ cosmic variance scaling below which errors are undetectable (see text).

B. Total dark matter

In the range $m \gtrsim 10^{-27}$ eV, the CMB and linear large-scale structure allow ULAs to compose a significant fraction of the dark matter. We take $f_{DM} = 1$ (well above observational limits in the nonlinear regime, which rule out $f_{DM} = 1$ for $m \lesssim 10^{-20}$ eV [61]) to illustrate the most extreme phenomenology and stringent tests of code accuracy.

In the $f_{DM} = 1$ case, the ULA density fluctuations are sharply cut off below its maximal Jeans scale (see Eq. A3). Here we show the $10^{-26} - 10^{-24}$ eV range whereas the fuzzy dark matter regime of $10^{-18} - 10^{-24}$ eV is discussed in Appendix A and Fig. 22. When $m < 10^{-26}$ eV as shown in Fig. 8 (top panel), this Jeans scale exceeds the nonlinear scale of Λ CDM, which corresponds to $k \sim 10^{-1}$ Mpc. To form bound structures at all, ULAs at lighter masses can no longer comprise most of the dark matter. Correspondingly as the mass decreases, the ULAs become more relevant to the primary CMB anisotropy as shown in Fig. 9. The stabilization of ULA density perturbations then change the metric perturbations which drive acoustic oscillations (see e.g. [34]), much like with neutrinos or dark radiation. For $m \lesssim 10^{-26}$ eV, this effect or its ISW analogue after recombination is so large that $f_{DM} = 1$ is immediately ruled out by CMB data just by inspection of these modifications to the shape of the spectrum (see Figs. 9 and 18)

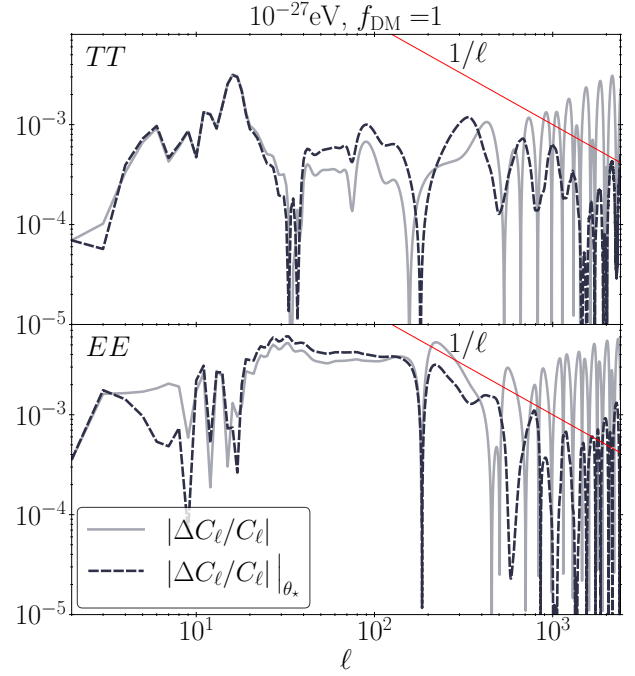


FIG. 10. $\Delta C_\ell/C_\ell$ for TT and EE before (light solid curve) and after the linearized correction (dashed curve) for the shift in the angular scale of the sound horizon $\Delta\theta_*/\theta_* = -2.7 \times 10^{-4}$ (see Eq. 41) for $m = 10^{-27}$ eV, $f_{DM} = 1$. Most of the error at high ℓ is due to this tiny shift, which does not significantly influence other cosmological inferences.

for the significance of the deviation from Λ CDM.).

Also shown in Figs. 8 and 9 are errors between AxIECAMB vs. the high accuracy calculation. The error in the transfer function ΔT_{rel} remains well below 10^{-2} across this range and is only mildly increasing as the mass decreases. This corresponds to ΔS_8 errors below 10^{-3} (see Tab. I). S_8 itself drops substantially for masses lower than $\sim 10^{-26}$ eV.

Likewise for C_ℓ^{TT} , it is only toward this ruled-out lower range of $10^{-26} - 10^{-27}$ eV that the $f_{DM} = 1$ errors exceed the $1/\ell$ line and differ noticeably from Λ CDM errors (see Fig. 6). The corresponding values of $\Delta\chi^2_{TT}$ values are given in Table I and do exceed unity there. EE and TE polarization power spectra errors are qualitatively similar to temperature but the stronger features in polarization lead to a more significant error in $\Delta\chi^2$ when compared with cosmic variance limits (see also Fig. 10).

For the most extreme case of $m = 10^{-27}$ eV the large $\Delta\chi^2$ indicates that in principle there could be a $\sqrt{\Delta\chi^2} \approx 7\sigma$ error in the analysis of such cosmic variance limited data. In fact, most of this error is associated with a very small shift in the background expansion and hence a very small change in the angular size of the sound horizon θ_* . In this example, the AxIECAMB calculation produces a shift of $\Delta\theta_*/\theta_* = -2.7 \times 10^{-4}$ compared with the high accuracy calculation. This small shift is statistically significant compared with the projected Fisher

m/eV	f_{DM}	S_8	$\Delta S_8/10^{-4}$	$\Delta \chi_{TT}^2$	$\Delta \chi^2$	$\Delta \chi^2 _{\theta_*}$	$(\Delta \theta_*/\theta_*)/10^{-5}$
—	0	0.85	1.6	0.20	0.47	—	—
10^{-24}	1	0.84	1.9	0.20	0.47	0.46	0.07
10^{-25}	1	0.72	-4.2	1.0	1.8	1.8	0.30
10^{-26}	1	0.36	-9.5	1.5	4.2	4.3	-5.0
10^{-27}	1	0.12	-5.9	5.8	53	2.6	-27
10^{-28}	0.1	0.55	0.69	0.53	1.3	0.75	3.2
10^{-29}	0.1	0.55	0.85	0.18	0.56	0.55	0.55
10^{-30}	0.1	0.59	0.95	0.18	0.59	0.55	0.85
10^{-31}	0.1	0.63	1.0	0.21	0.66	0.52	1.8

TABLE I. Example ULA models, observables and errors between AxiECAMB and the high accuracy calculation. The entry for $f_{\text{DM}} = 0$ is the ΛCDM benchmark model.

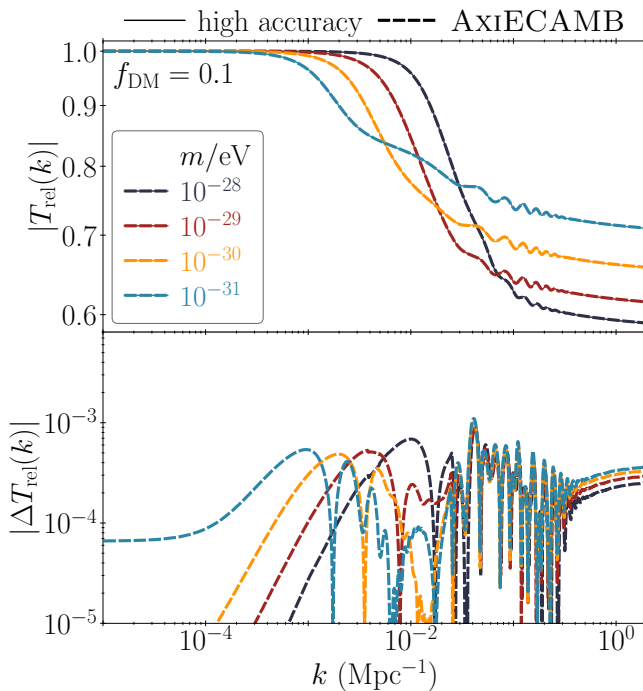


FIG. 11. Relative transfer function $T_{\text{rel}}(k)$ (top) for fractional dark matter cases ($f_{\text{DM}} = 0.1$) and errors between the AxiECAMB and high accuracy computations (bottom).

errors on this single parameter $\sigma_{\ln \theta_*} = 4.1 \times 10^{-5}$. Compared with the *Planck* 2018 TT , TE , EE actual errors of $\sigma_{\ln \theta_*} \sim 3 \times 10^{-4}$ [52], this forecast is a factor of 7 better. For other cases, the improvement is at least a factor of 5 in errors or a factor of 25 in the implied reduction of $\Delta \chi^2$. Furthermore, cosmological parameter estimation based on the distance to the recombination surface is already limited by uncertainties in the sound horizon r_* , not measurement errors in $\ln \theta_*$. The *Planck* 2018 errors for the former are much larger, $\sigma_{\ln r_*} = 2 \times 10^{-3}$. Therefore, shifts of $\Delta \theta_*/\theta_* \sim 10^{-4}$ from our default accuracy calculation would not significantly impact cosmological parameter errors based on distance inferences like H_0 at

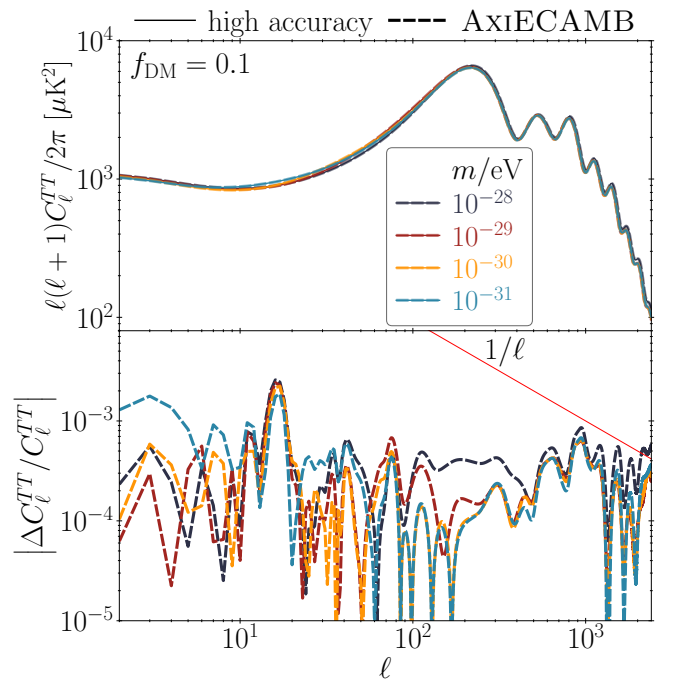


FIG. 12. C_ℓ^{TT} in the fractional dark matter cases (top; $f_{\text{DM}} = 0.1$) and its fractional error between AxiECAMB and high accuracy calculations as in Fig. 9.

the present or even in the foreseeable future.

To see that this θ_* shift captures the main source of the $\Delta \chi^2$ error as well, we can approximately correct this error in the acoustic regime of CMB primary anisotropy by an equivalent shift in the multipole spectrum

$$\Delta C_\ell(\text{corrected}) = \Delta C_\ell(\text{original}) - \left[\frac{\Delta \theta_*}{\theta_*} \frac{dC_\ell}{d \ln \ell} \right]. \quad (41)$$

In Fig. 10, we show that with this correction, the errors for $m = 10^{-27} \text{ eV}$ and $f_{\text{DM}} = 1$ are reduced below the CV line for TT and comparable to it for EE ; correspondingly $\Delta \chi^2|_{\theta_*} = 2.6$ where $|_{\theta_*}$ denotes the remaining errors after fixing θ_* in this manner.

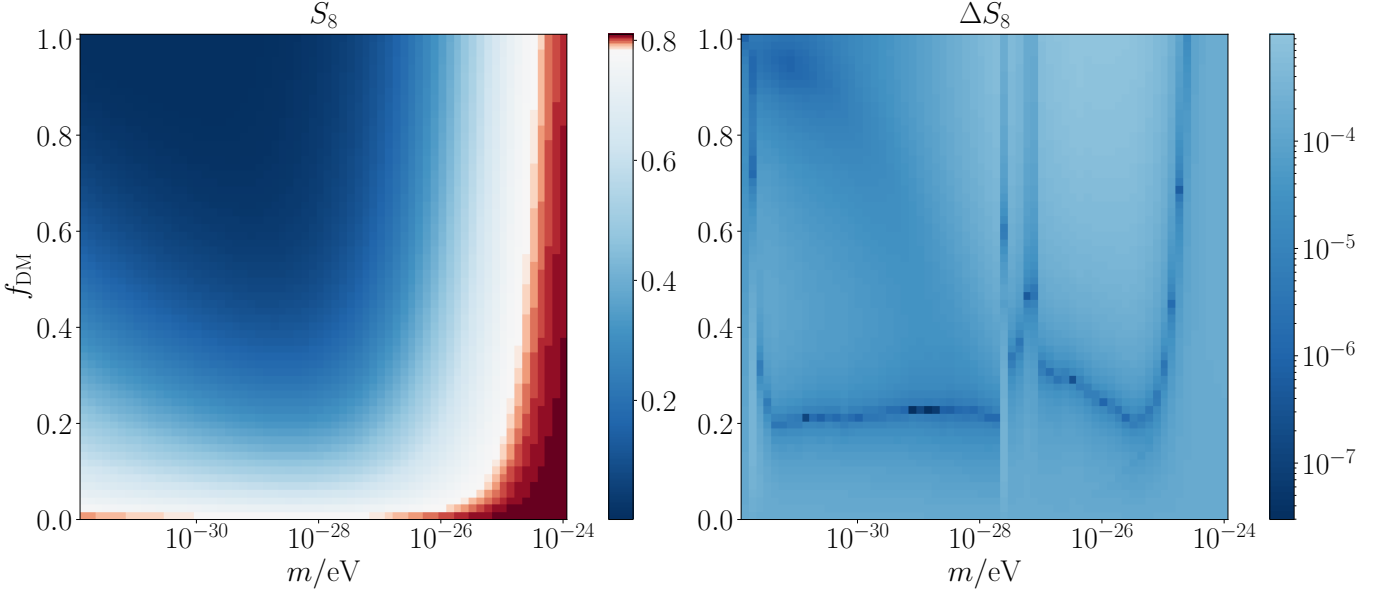


FIG. 13. Large scale structure amplitude S_8 (left) in the m, f_{DM} plane and its error ΔS_8 between AxI^ECAMB and high accuracy computations.

C. Fractional dark matter

For the mass range $10^{-31} < m/\text{eV} < 10^{-28}$, the ULAs can only comprise a small fraction of the dark matter. Current constraints from the linear regime require $f_{\text{DM}} \lesssim 0.05$ (95% CL) [42] and so for illustration purposes we take $f_{\text{DM}} = 0.1$ to highlight the accuracy of the approach in the most extreme case that is relevant for parameter estimation.

The relative transfer function shown in Fig. 11 (top panel) has a sharp decrease at the ULA Jeans scale but then stabilizes at higher k due to the presence of CDM. The suppression at high k results from the slower growth of CDM fluctuations due to the effect of the background ULA density, much like the effect of massive neutrinos (see e.g. [62]). The errors in ΔT_{rel} are below the 10^{-3} level and are sufficiently small for current and near future constraints. Correspondingly, the ΔS_8 error in Tab. I is below 10^{-4} even though S_8 itself is significantly reduced by the ULA suppression of growth to $S_8 \sim 0.5 - 0.6$.

In Fig. 12 we show the corresponding CMB temperature anisotropy. Even without the correction for θ_* , the error is at or below the CV line for these $f_{\text{DM}} = 0.1$ cases and correspondingly both $\Delta\chi^2_{TT}$ and $\Delta\chi^2$ is order unity or below (see Tab. I). For the lighter masses in this range, the main effect of the ULA is to raise the early ISW effect at multipoles before the first peak. The θ_* correction makes a negligible difference for these models since the shift is only $\sim 10^{-5}$.

For a comprehensive understanding of the errors across the full m and f_{DM} space, we evaluate S_8 and its errors in Fig. 13. The errors are everywhere $< 10^{-3}$ and peak around $m \sim 10^{-28} \text{ eV}$. For lighter masses, the ULA density fluctuations have not caught up by the present

with the baryons for $f_{\text{DM}} = 1$ and CDM fluctuations for lower f_{DM} at $k \approx 0.1 \text{ Mpc}^{-1}$ and thus impact S_8 as a homogeneous background that suppresses the growth as described above. Thus errors in the ULA density fluctuations themselves become less relevant for S_8 (see also the discussion of Figs. 20, 26).

Likewise, we show $\Delta\chi^2$ and $\Delta\chi^2|_{\theta_*}$ in Fig. 14. The main error ‘hotspot’ in the left panel is just above the lightest in the DM-like mass range with the extreme $f_{\text{DM}} \rightarrow 1$, which is in the grossly ruled out region of being most to all of the dark matter, and correcting for the contribution of θ_* reduces $\Delta\chi^2$ to low levels compared with CV even in this region.

Despite being the main source of error in CMB spectra, the maximum error is $\Delta\theta_*/\theta_* \sim 9 \times 10^{-4}$, which occurs around $m = 10^{-31} \text{ eV}$, $f_{\text{DM}} = 1$. Larger errors occur in this region since the switch takes place at low redshifts $z_* \sim 4$ when the resulting change in the expansion rate has its maximal effect on the distance to the recombination surface, and hence θ_* . As $m \rightarrow 10H_0$ (left edge of Fig. 14), the switch of both the default and high accuracy calculations is at $z = 0$ and the difference between the two diminishes, albeit in an oscillatory fashion that depends on the phase of the KG oscillation at $z = 0$.

Other features in the $m \gtrsim 10^{-28} \text{ eV}$ range highlight the strategy taken in Sec. II D for boosting the default m/H_* above the baseline of 10. The vertical stripes near $m \sim 10^{-27.5} \text{ eV}$ represent the mass range where the baseline switch would have occurred in the recombination window but is raised by our approach to beyond it (see Fig. 28). Around these masses and $f_{\text{DM}} = 1$, the main errors are again shifts in θ_* , here due to the sound horizon r_* , as the θ_* correction shows. In fact, most of the r_* error when the switch is after recombination comes from our

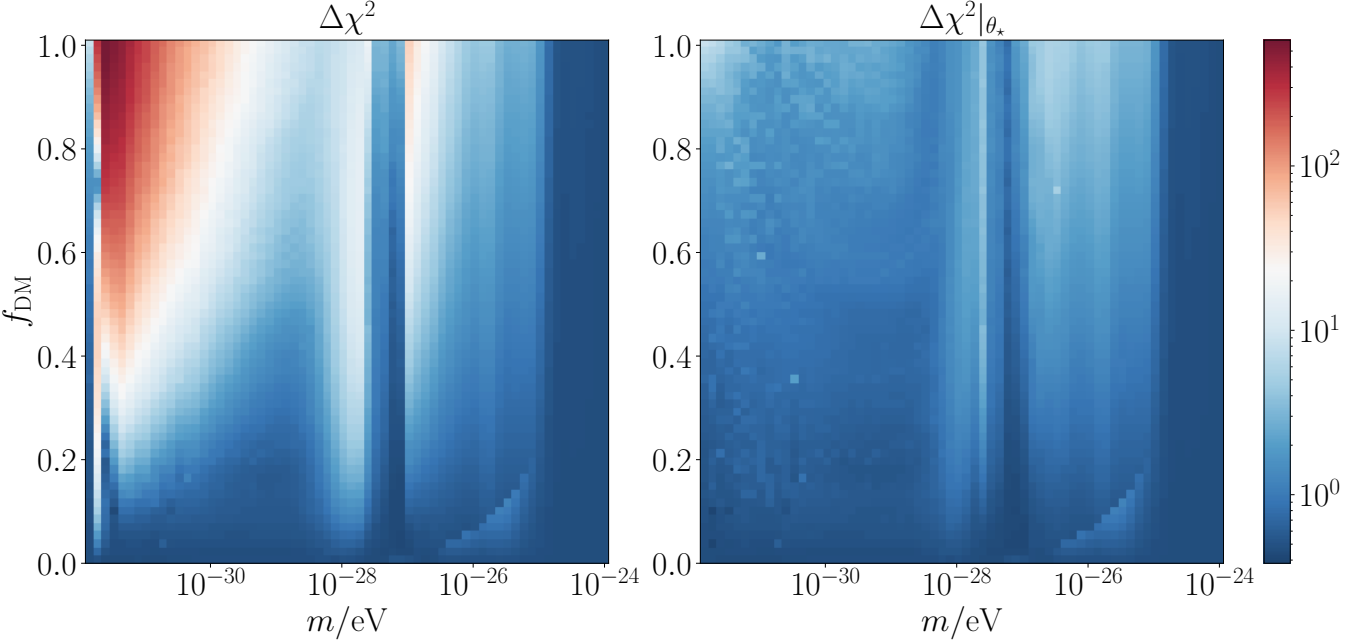


FIG. 14. CMB accuracy statistic $\Delta\chi^2$ in the $m - f_{\text{DM}}$ plane (left panel). The dominant error is removed by correcting for the very small change in the angular scale of the sound horizon (right panel) (see Fig. 10).

convention that $\Omega_{\text{ax}}h^2$ is fixed rather than the initial field value ϕ_{ini} . The impact of this shift is at most a $\lesssim 10^{-3}$ change in the value of $\Omega_{\text{ax}}h^2$ corresponding to a given CMB prediction.

The curve around $f_{\text{DM}} = (m/10^{-23.5}\text{eV})^{1/2}$ between $10^{-27.5} < m/\text{eV} < 10^{-25}$ is due to the boosting of m/H_* in the ULA-radiation equality window. The tuning of the phase of this switch is to $m = 10^{-26}\text{ eV}$ and improves the errors in this mass range.

D. Total dark energy

For $m < 10^{-32}\text{ eV}$, $m/H_0 \lesssim 10$ and the KG field is not highly oscillating at the present. In this scenario the ULA behave as a quintessence dark energy field and AxIECAMB solves the KG system all the way to the present. In our examples we take $f_{\text{DE}} = 1$ and consider the ULA as all of the dark energy.

As part of the dark energy, we exclude ULA in T_m but the ULA still impacts the growth of matter fluctuations and hence T_{rel} below the Jeans scale if the field ϕ rolls substantially before the present. In Fig. 15 we show the ULA effect on T_{rel} , and that the errors are comparable to those of the transfer function in ΛCDM itself. Here $S_8 = 0.46, 0.77$ and 0.84 for $m/\text{eV} = 10^{-32}, 10^{-32.5}, 10^{-33}$ respectively.

The corresponding CMB TT spectra are plotted in Fig. 16. Here the main effects on the CMB is through the change in the late ISW effect and the low redshift distance redshift relation. We see once again that our AxIECAMB is accurate to the same level as the ΛCDM

calculation with $\Delta\chi^2 = 0.96, 0.53$ and 0.47 for the three cases respectively. There is no analogue to a θ_* correction from the switch in this range since both high and low accuracy calculations solve the KG system to the present.

IV. DISCUSSION

We have developed a method and publicly available code AxIECAMB for the fast and accurate solution of ultralight axion perturbations across the whole mass range from the fuzzy dark matter regime of 10^{-18} eV to the frozen dark energy regime of 10^{-33} eV . The method switches from solving the Klein-Gordon equation to an effective fluid once the mass oscillations become sufficiently rapid compared with the Hubble rate $m/H \geq m/H_*$. At the switch, the matching conditions are established through an effective time average of the impact of the KG oscillations on the background and perturbations.

Our baseline choice of switch time $m/H_* = 10$ is sufficiently accurate for subpercent accuracy predictions for CMB and matter power spectra, and the accuracy is efficiently improved by increasing this value. In fact the main source of this error in the CMB is a small fractional shift in the angular size of the sound horizon that is no more than 9×10^{-4} even in the most extreme case of models which are not observationally viable. Aside from this shift, which should not affect cosmological parameter estimation in the foreseeable future, the default accuracy approaches the cosmic variance limit at $\ell_{\text{max}} = 2400$, comparable to ΛCDM calculations.

Our method improves on previous approaches in a

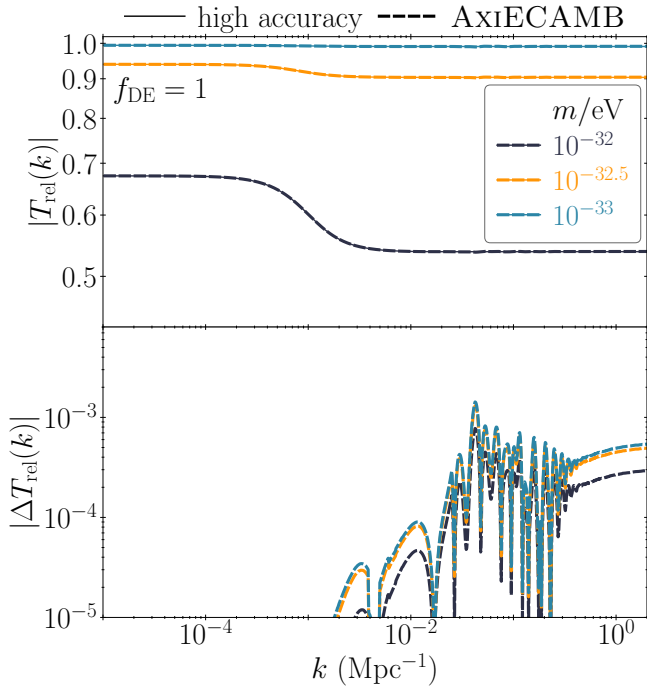


FIG. 15. Relative transfer function for total dark energy cases ($m < 10H_0$, $f_{\text{DE}} = 1$) and errors between AxIECAMB and high accuracy computations. Here the matter components of the relative transfer function do not include the ULA.

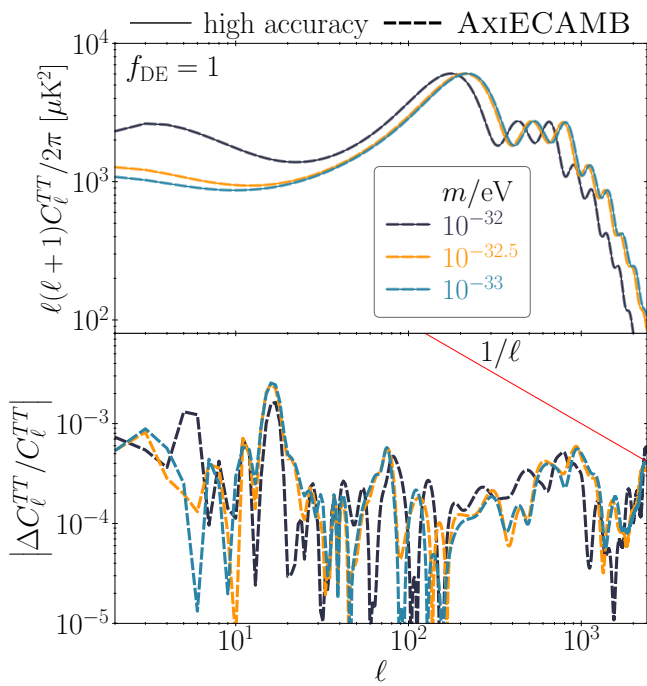


FIG. 16. C_ℓ^{TT} for total dark energy cases ($m < 10H_0$, $f_{\text{DE}} = 1$) and fractional errors between AxIECAMB and high accuracy computations.

number of ways. By developing the ETA of both the matter and metric variables, we achieve high accuracy for the low mass regime where the switch occurs near or after matter-radiation equality. This construction removes the leading order oscillations in these variables and provides $\mathcal{O}(H_*^2/m^2)$ or better accuracy in the matter and CMB observables even when the ULAs comprise all of the dark matter. Since the ETA holds for any phase of the KG oscillations, it establishes continuity to leading order with the EFA simultaneously in all of the variables, including the pressure and its fluctuation, unlike methods that match the ULA density field at a specific point. This method eliminates spurious pressure wave oscillations below the ULA Jeans scale and allows the accuracy of CMB power spectra to be further improved through a choice of the switch phase that reduces higher order effects in the regime around equality, $10^{-28} \lesssim m/\text{eV} \lesssim 10^{-25}$. We also account for boundary terms in CMB anisotropy source functions that arise from the switch or any background curvature.

As we show in Appendix A when compared with AXIONCAMB, in certain regions of parameter space, far from ΛCDM , the improvements in $\Delta\chi^2$ error can reach 5 orders of magnitude. In regions closer to ΛCDM , AXIONCAMB can still be in error by a significant fraction of the change from ΛCDM . While our improvements are unlikely to change cosmological constraints on ULAs qualitatively, the order unity (and thus possibly relevant for *Planck* constraints) inaccuracy of the ULA change from ΛCDM in certain regions of parameter space merits further study. Similarly we have improved upon AXIONCAMB and fitting functions for the transfer function in the fuzzy dark matter regime $10^{-24} < m/\text{eV} < 10^{-18}$ but the changes are quantitative rather than qualitative. Finally, our improvements on both the method and numerical implementation collectively decreased the run time by $\sim 50\%$ compared to AXIONCAMB in spite of the much higher accuracy, and is comparable to the speed of CAMB in ΛCDM .

While we implemented our method specifically for a ULA potential with a purely quadratic form, our technique can be readily extended for cases with self interactions by moving the switch time to be when the quadratic approximation holds around the minimum. Our method can also be applied to ULA isocurvature perturbations. We leave these and other considerations for future work.

ACKNOWLEDGMENTS

We thank T. L. Smith, D. J. E. Marsh, R. Hložek, S. Passaglia, H. Winch, and T. Cookmeyer for useful discussions. R.L. and W.H. were supported by U.S. Dept. of Energy contract DE-FG02-13ER41958 and the Simons Foundation. D.G. acknowledges support from the Charles Kaufman foundation through grant KA2022-129518, and the provost's office at Haverford College.

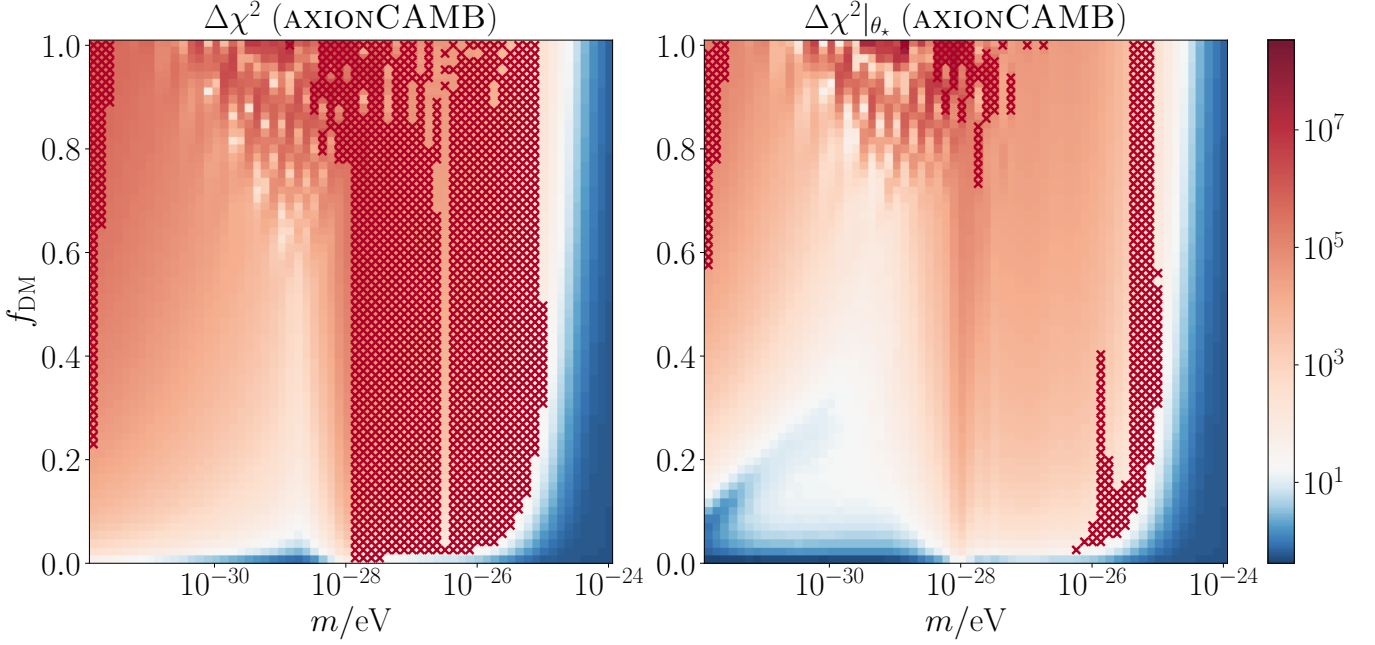


FIG. 17. $\Delta\chi^2$ errors for AXIONCAMB relative to our high accuracy computation before (left) and after (right) the correction for θ_* as in Fig 14. “ \times ” marks are placed on regions where the error $\Delta\chi^2 > 25$ and exceeds $\Delta\chi^2(\Lambda\text{CDM})/2^2$, the deviation of ΛCDM from the model.

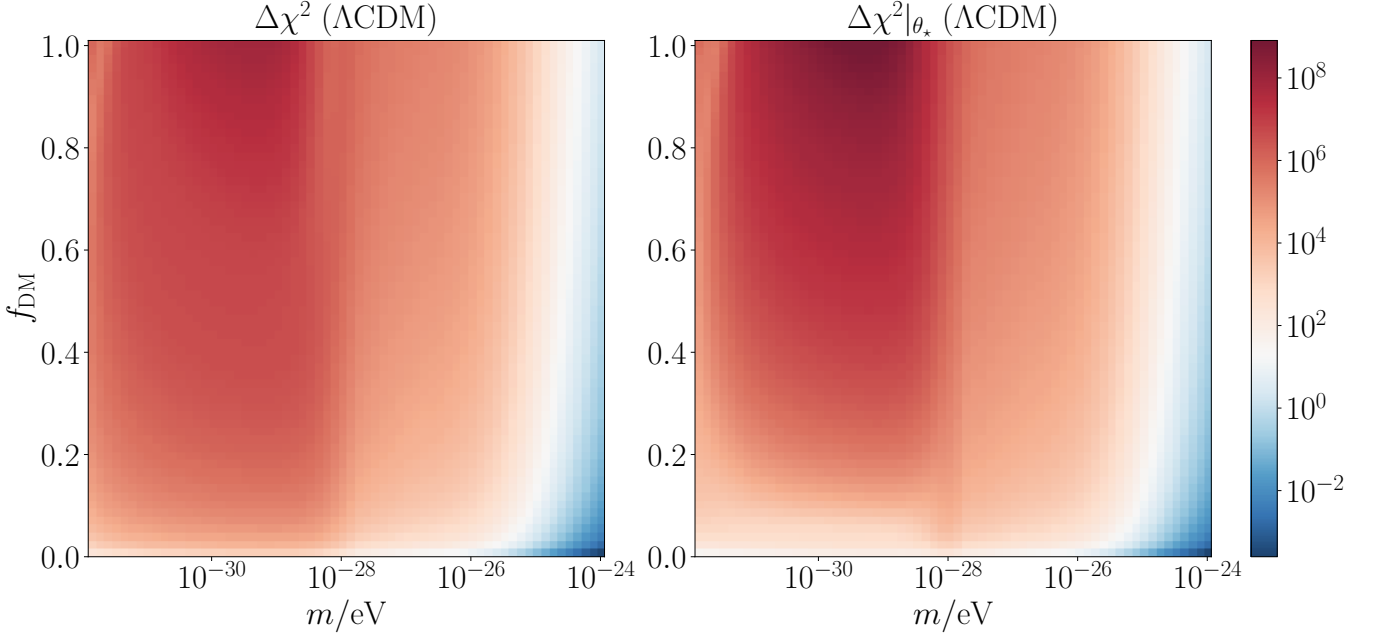


FIG. 18. $\Delta\chi^2(\Lambda\text{CDM})$, the significance of the difference between ΛCDM and the ULA model, before (left) and after (right) the linearized correction for the different θ_* using Eq. (41). In regions where the model error in Fig. 17 are comparable to these differences, the effect of ULAs are not accurately computed.

Appendix A: Comparison with Previous Work

We compare the predictions of AxieCAMB with previous codes, primarily AXIONCAMB. Our code was developed by extensively modifying and rewriting AXION-

CAMB (and consequently shares the same 2013 CAMB code base). It thus provides a fair comparison of errors induced by previous fluid approximation techniques. We show regions of parameter space where power spectra are inaccurately computed in AXIONCAMB, which implies

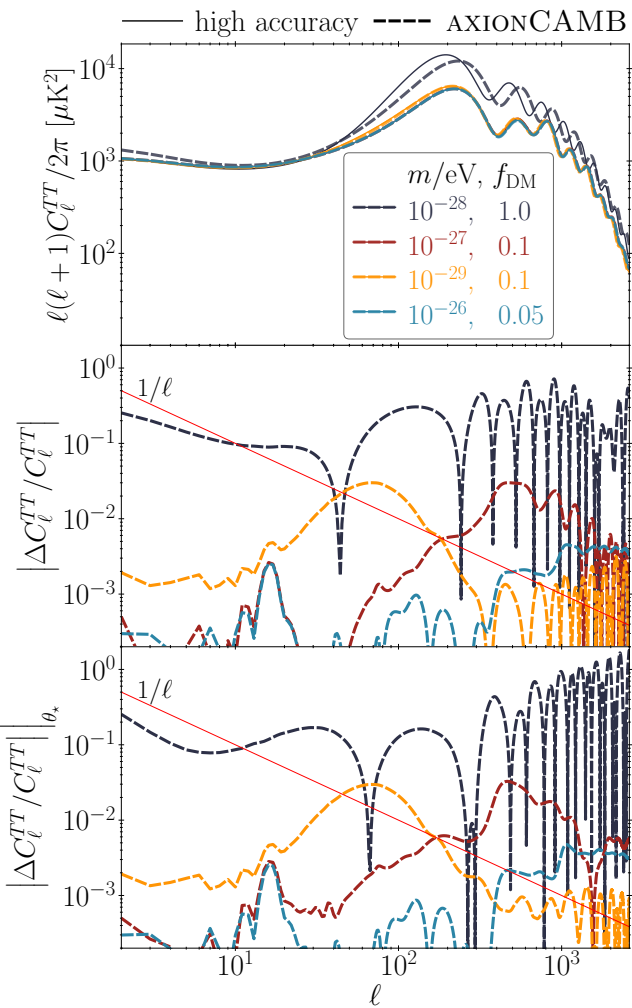


FIG. 19. C_ℓ^{TT} errors in AXIONCAMB compared with the high accuracy calculation, taken from different representative regions in Fig. 17 (see text). Errors here are much larger than in AxIECAMB (cf. Sec. III) and only partially mitigated by the linear correction in the θ_* shift.

that existing constraints should be re-examined in light of these improvements. We also compare with the transfer function fits from Ref. [45] in the fuzzy dark matter regime of $10^{-24} < m/\text{eV} < 10^{-18}$. In this appendix we always use the high accuracy version of our calculations for comparison as in the main text.

AXIONCAMB solves for the ULA perturbations before a switch at $m/H_* = 3$ using the generalized dark matter (GDM) fluid approach [30] instead of the field perturbations. Rather than introducing an explicit switch partitioning between the GDM and EFA, it simply changes the equation of state and sound speed discontinuously at $m/H_* = 3$ and integrates the same fluid-like system across the whole evolution. While the GDM description is exactly equivalent to the Klein-Gordon equation, it cannot be solved to much higher switch values due to divergences in the adiabatic sound speed $\dot{\rho}_{\text{ax}}/\dot{\rho}_{\text{ax}}$ once the

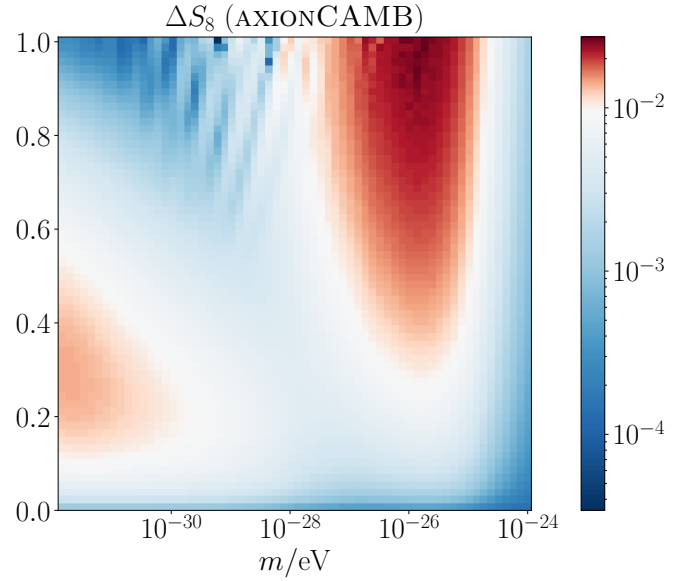


FIG. 20. ΔS_8 errors in AXIONCAMB relative to our high accuracy calculation. Errors peak at a few 10^{-2} and are much larger than those for AxIECAMB (cf. Fig. 13).

KG field starts oscillating whereas the change to the EFA fluid eliminates this problem.

We begin by computing $\Delta\chi^2$ between CMB power spectra obtained from AXIONCAMB and our high-accuracy calculation. The results using the same accuracy metrics defined in Sec. IIIA are shown in Fig. 17. The $\Delta\chi^2$ errors for AXIONCAMB reach values of $\mathcal{O}(10^7)$ in certain regions of the $m - f_{\text{DM}}$ parameter space whereas AxIECAMB errors peaks at $\mathcal{O}(10^2)$. Though correcting for errors in θ_* using the linearized shift of Eq. (41) does improve AXIONCAMB errors in some regions of the space, they remain much higher than in AxIECAMB.

For reference, we also plot $\Delta\chi^2(\Lambda\text{CDM})$, the $\Delta\chi^2$ deviation between ΛCDM and our high accuracy calculation in Fig. 18 before (left panel) and after (right panel) correction for the different θ_* using Eq. (41). Note that the linearized correction only reduces the difference when $|\Delta\theta_*/\theta_*| \ll 0.1$, given the spacing $\Delta\ell$ between the acoustic peaks and $\ell_{\text{max}} = 2400$. Instead the correction makes the difference artificially larger near 10^{-29} eV and $f_{\text{DM}} \sim 1$ but this is not the regime of interest for allowable deviations from ΛCDM . Many of the largest errors in AXIONCAMB also occur in such regions.

To identify the more problematic regions for the use of AXIONCAMB in parameter constraints, we place cross marks in Fig. 17 on parameter points that pass the joint thresholds

$$\begin{aligned} \Delta\chi^2(\text{AXIONCAMB}) &> 25, \\ \Delta\chi^2(\text{AXIONCAMB}) &> \left(\frac{1}{2}\right)^2 \Delta\chi^2(\Lambda\text{CDM}), \end{aligned} \quad (\text{A1})$$

where the 1/2 value is a loose, arbitrarily chosen thresh-

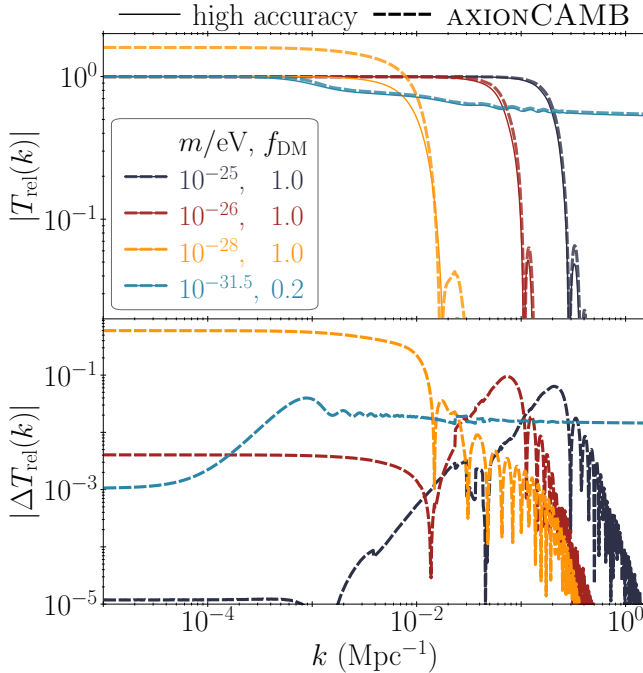


FIG. 21. $T_{\text{rel}}(k)$ (top) and $\Delta T_{\text{rel}}(k)$ (bottom) comparing AXIONCAMB (dashed) with that run on high accuracy setting (solid), for representative cases in Figs. 17 and 20.

old to reflect an error of half the change in the CMB power spectra C_ℓ from ΛCDM .⁷

The source of errors causing both large $\Delta\chi^2$ values and inaccurate depiction of the change from ΛCDM can be examined on a case-by-case basis. There are at least 4 distinct types of behavior which we illustrate in Fig. 19. The first is the wildly fluctuating errors near $m = 10^{-28} \text{ eV}$ and $f_{\text{DM}} = 1$. Here $\Delta C_\ell^{TT}/C_\ell^{TT}$ approaches $\mathcal{O}(1)$ indicating grossly inaccurate calculations.

We have identified that in this region the AXIONCAMB solution for the initial field ϕ_{ini} can fail badly as it fits the logarithm of the ULA fraction of matter as a function of ϕ_{ini} with spline interpolation to invert the relation. This function saturates as $\phi_{\text{ini}} \rightarrow \infty$, and so the fit fails. In some cases, due to precision, the implementation in AXIONCAMB even introduces a zero or nonmonotonic spacing of spline steps resulting in NaN outputs, which we fix to produce Fig. 17. AxiECAMB avoids this failure by finding the correct ϕ_{ini} by bisection, given $\Omega_a h^2$ instead of the problematic ULA fraction.

⁷ To assess the significance of the error between AXIONCAMB and our high-accuracy computation, we use the threshold $\Delta\chi^2 = 25$ rather than 1 to roughly reflect current rather than future constraints. In Sec. III B, we found that the future CV limit improves on θ_* errors by at least a factor of ~ 5 over *Planck* errors. Note however that this scaling only applies to cases where the dominant error is at high ℓ since *Planck* is already CV-limited at low ℓ in TT.

While this is mainly a background error, it is so large that it cannot be corrected with θ_* as in Eq. (41). With $m = 10^{-28} \text{ eV}$ and $f_{\text{DM}} = 1$ in particular, $\Delta\theta_*/\theta_* = -0.16$, $\Delta\chi^2 = 2.8 \times 10^6$ and $\Delta\chi^2|_{\theta_*} = 2.6 \times 10^7$, indicating a breakdown of the linearized θ_* correction. While a nonlinear correction could potentially improve $\Delta\chi^2$, the error still indicates a substantial misvaluation in distance-related observables in this regime such as H_0 .

Secondly, in the lower f_{DM} region near the example model with $m = 10^{-27} \text{ eV}$ and $f_{\text{DM}} = 0.1$, errors of $\Delta C_\ell^{TT}/C_\ell^{TT}$ are around a few percent in the currently well measured acoustic regime. The errors cannot also be fully corrected with $\Delta\theta_*/\theta_*$, as seen in the example model where $\Delta\theta_*/\theta_* = 0.0011$, $\Delta\chi^2 = 1109$ and $\Delta\chi^2|_{\theta_*} = 638$. Moreover, the error is a significant fraction of the difference from ΛCDM : $\sqrt{\Delta\chi^2/\Delta\chi^2(\Lambda\text{CDM})} = 0.54$, and 0.40 after the θ_* correction. Such an error can make a large fractional change in ULA parameter constraints from the CMB.

Thirdly, near $m = 10^{-29} \text{ eV}$ and $f_{\text{DM}} = 0.1$, there remains errors of a few percent in $\Delta C_\ell^{TT}/C_\ell^{TT}$, whose scale has shifted however to lower multipoles and contributes less to $\Delta\chi^2$, although still above cosmic variance in the range where *Planck* is CV limited. Larger contributions to $\Delta\chi^2$ at high ℓ are correctable with $\Delta\theta_*/\theta_* = -3 \times 10^{-4}$, with $\Delta\chi^2 = 68$ and $\Delta\chi^2|_{\theta_*} = 14$. This case also shows an error that is small compared with the difference from ΛCDM : $\sqrt{\Delta\chi^2/\Delta\chi^2(\Lambda\text{CDM})} = 0.017$ before and ≈ 0.037 after correction for $\Delta\theta_*/\theta_*$.

Finally, a long strip of \times 's appears in the right panel of Fig. 17 between $10^{-26} - 10^{-25} \text{ eV}$. For the model at its lowest f_{DM} end, $m = 10^{-26} \text{ eV}$ and $f_{\text{DM}} = 0.05$, $\Delta\chi^2 = 80$, $\Delta\chi^2|_{\theta_*} = 71$, and $\sqrt{\Delta\chi^2/\Delta\chi^2(\Lambda\text{CDM})} \approx 0.54$ before θ_* correction and a negligibly better 0.51 after. This model is around the mass and f_{DM} where the CMB becomes the dominant current constraint [42], and such an error can shift constraints quantitatively.

In Fig. 20 we show the errors in S_8 as ΔS_8 .⁸ We highlight specific models where the relationship between ΔS_8 and the various sources of matter power spectrum error can be better understood in Fig. 21 for $T_{\text{rel}}(k)$.

The ΔS_8 errors peak around $m = 10^{-26} \text{ eV}$ and $f_{\text{DM}} = 1$, where $S_8 = 0.36$ and $\Delta S_8 = 0.027$. Here the ULA Jeans scale is comparable to the scale of S_8 and the peak error in ΔT_{rel} has its maximal impact.

Another local peak in ΔS_8 occurs at very light masses and intermediate f_{DM} . As an example we take $m = 10^{-31.5} \text{ eV}$ and $f_{\text{DM}} = 0.2$, where $S_8 = 0.5$ and $\Delta S_8 = 0.013$. This error is attributed to the $\Delta T_{\text{rel}} \sim 10^{-2}$ errors at high k below the Jeans scale where the smooth ULA background slows the growth of CDM fluctuations. For much larger f_{DM} , T_{rel} is so small that even large

⁸ AXIONCAMB uses a different definition of σ_8 that is not always the matter density rms defined by our T_m in Eq. (39). We calculate the S_8 from AXIONCAMB consistent with our definition here.

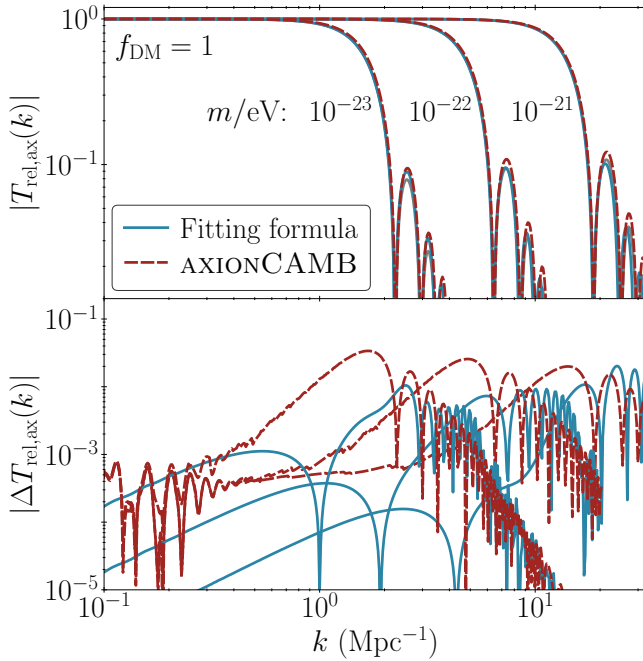


FIG. 22. Relative transfer function in the fuzzy dark matter regime $T_{\text{rel,ax}} = T_{\text{ax}}/T_c$ (gray, high accuracy, see text). The errors for AXIONCAMB and a fitting function from Ref. [45] are shown in the bottom panel.

fractional errors in its value lead to small ΔS_8 despite being large fractional errors in S_8 itself. There are also spurious oscillations below the Jeans scale between $k = 10^{-3} - 10^{-2}$ Mpc $^{-1}$ which are the consequence of the very large quasistatic equilibrium violation in the ULA that are masked by the much larger CDM and baryon density fluctuations that contribute to T_{rel} (see Fig. 26).

In the regime around $m = 10^{-28}$ eV and $f_{\text{DM}} = 1$ that we studied for C_ℓ , the same background errors in ϕ_{init} cause $\mathcal{O}(1)$ errors in the low k amplitude of $T_{\text{rel}}(k)$. On the scales relevant to S_8 , these problems produce a $\Delta S_8 = 0.013$ for $S_8 = 0.031$ and a large fractional error despite the model itself being ruled out by its inability to form nonlinear structure regardless of this error.

For a model closer to Λ CDM, we take $m = 10^{-25}$ eV, $f_{\text{DM}} = 1$, where $S_8 = 0.72$ and $\Delta S_8 = 0.018$, which is a small but non-negligible fraction of the change from the Λ CDM value of 0.85.

Apart from the above study of masses below 10^{-24} eV where the ULA Jeans scale is on cosmological scales, we examine the fuzzy dark matter region where the Jeans scale is instead on astrophysical scales. Here the transfer function is mainly used to set up initial conditions of the ULA for nonlinear simulations. We therefore exclude the baryons and massive neutrinos from the matter transfer function and take its ratio with the cold dark matter transfer function to define $T_{\text{rel,ax}} = T_{\text{ax}}/T_c(f_{\text{DM}} = 0)$ for $f_{\text{DM}} = 1$. In Fig. 22 we plot this quantity and its errors $\Delta T_{\text{rel,ax}}$ from AXIONCAMB, which slightly underestimates the Jeans scale leading to an over-estimate

of the transfer function in this regime which peak at $\Delta T_{\text{rel,ax}} \sim 10^{-2}$. Most of this difference would be absorbed into a small shift in m . AxiECAMB on the other hand performs similarly or better than that shown for 10^{-24} eV in Fig. 8 so that these errors are reduced to 10^{-3} or below. While not shown in Fig. 8 for clarity reasons, they are entirely negligible for simulation purposes.

We also compare in Fig. 22 the errors from a fitting function of $T_{\text{rel,ax}}$ from Ref. [45]:

$$T_{\text{rel,ax}}(k) \simeq \frac{\sin(x^n)}{x^n(1 + Bx^{6-n})}, \quad (\text{A2})$$

where [30]

$$x \equiv A \frac{k}{k_J}, \quad k_J = 9m_{22}^{1/2}, \quad (\text{A3})$$

with $m_{22} \equiv m/10^{-22}$ eV, $n = 5/2$, and

$$\begin{aligned} A &= 2.22m_{22}^{1/25-1/1000 \ln(m_{22})}, \\ B &= 0.16m_{22}^{-1/20}. \end{aligned} \quad (\text{A4})$$

Here most of the amplitude error in $\Delta T_{\text{rel,ax}}$ compared with AXIONCAMB is removed, leaving mainly a phase error in the Jeans oscillations at high k . Since phasing differences would be destroyed in nonlinear evolution, the fitting function should thus also provide sufficiently accurate initial conditions for numerical simulations.

While the AxiECAMB method works for $m > 10^{-18}$ eV, the Jeans scale moves into the $k_J \gtrsim 10^3$ Mpc $^{-1}$ regime where non-ULA perturbations also are difficult to track. In this regime, the fitting function is a more efficient means of providing initial conditions for simulations.

Appendix B: KG solutions and scalings

Here we discuss field solutions for the KG system that are useful in establishing our effective method for the background and perturbations.

For the background, the field has an exact solution when the expansion history can be described by a constant total equation of state w_T (e.g. Ref. [24]):

$$\phi \propto a^{-3/2} \sqrt{mt} J_\nu(mt), \quad (\text{B1})$$

where

$$\nu = \frac{(1 - w_T)}{2(1 + w_T)}. \quad (\text{B2})$$

The Bessel function takes the limiting form

$$\lim_{mt \ll 1} J_\nu(mt) \approx \frac{2^{-\nu}}{\Gamma(1 + \nu)} (mt)^\nu, \quad (\text{B3})$$

whereas in the opposite limit,

$$\lim_{mt \gg 1} J_\nu(mt) \approx \sqrt{\frac{2}{\pi mt}} \left(\cos \beta - \frac{4\nu^2 - 1}{8mt} \sin \beta \right), \quad (\text{B4})$$

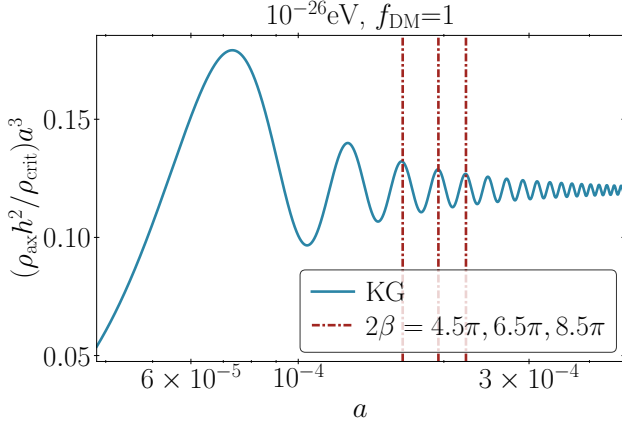


FIG. 23. Prediction of temporal location of peaks the KG oscillations in $\rho_{\text{ax}} a^3$ for a case where they occur around equality. Here $m = 10^{-26}\text{eV}$, $f_{\text{DM}} = 1$ and vertical lines represent the prediction for peaks peaks $n = 3, 4, 5$ where $2\beta = \pi/2 + 2\pi(n - 1)$ (see text for details).

with the evolving phase

$$\beta = mt - \nu\pi/2 - \pi/4. \quad (\text{B5})$$

Notice that for any w_T , $\phi = \text{constant}$ for $mt \ll 1$, consistent with a Hubble drag dominated solution. Conversely for $mt \gg 1$, i.e. $m/H \gg 1$, the amplitude of $\phi \propto a^{-3/2}$ to leading order, consistent with ULAs redshifting as matter.

In the radiation-dominated epoch, $w_T = 1/3$ and this solution in principle checks all of the steps of our effective method for $m \gg 10H_{\text{eq}}$. First of all here $Ht = 1/2$ and we can immediately verify the initial conditions for $\dot{\phi}$ in Eq. (4) as well as those of the perturbations given that $\dot{h} \propto \tau$. This applies to any mass since the initial conditions are always set in radiation domination. Next we can determine the ETA of the oscillations in the $m/H = 2mt \gg 1$ limit of Eq. (B4). Using the same approach of setting $\cos^2 \beta = \sin^2 \beta \rightarrow 1/2$ and $\cos \beta \sin \beta \rightarrow 0$, we obtain

$$w^{\text{ETA}} = \frac{9}{8}(1 + w_T) \left(\frac{H}{m}\right)^2, \quad (\text{B6})$$

and hence $w^{\text{ETA}} = (3/2)(H/m)^2$ in radiation domination, which implies $A_w = 3/2$ in Eq. (17). This value was adopted in Ref. [45] where $m \gg 10H_{\text{eq}}$ was assumed.

Given that the homogeneous equation of motion for the field perturbation is the same as the background for $k/am \rightarrow 0$ and in the radiation dominated epoch $\dot{h} \propto \tau$ is an external source, we can construct the inhomogeneous solution using the Green function technique to find

$$\lim_{k \rightarrow 0} \frac{\delta p_{\text{ax}}^{\text{ETA}}}{\delta \rho_{\text{ax}}^{\text{ETA}}} = \left[\frac{9}{8} w_T (1 + w_T) + 1 \right] \frac{H^2}{m^2}, \quad (\text{B7})$$

or $(3/2)(H/m)^2$ in radiation domination, which in principle specifies $A_c = 3/2$ in Eq. (20). As explained in the

main text, since we construct the ETA not from the analytic solution but rather from the auxiliary field construction, we follow Ref. [45] and use the empirical value of $A_c = 5/4$ determined from this construction for switches deep in radiation domination. In the opposite subhorizon regime, it is mainly the finite value of $k/am \gg H/m$ that causes the phase of the perturbations to differ from the background rather than the metric fluctuation. We can derive an ETA for the sound speed by ignoring the metric fluctuation and extracting the natural frequency of oscillation from the dispersion relation

$$\omega = \sqrt{k^2 + a^2 m^2}. \quad (\text{B8})$$

The phase of the field fluctuation differs from that of the background by

$$\begin{aligned} \delta\beta &= \int d\tau \omega - mt = \int d\tau (\omega - am) \\ &\equiv k \int d\tau c_\phi, \end{aligned} \quad (\text{B9})$$

where

$$c_\phi = \left(\frac{k}{am} \right)^{-1} \left[\sqrt{1 + \left(\frac{k}{am} \right)^2} - 1 \right]. \quad (\text{B10})$$

We can then repeat the ETA construction of $\delta p_{\text{ax}}^{\text{ETA}}/\delta \rho_{\text{ax}}^{\text{ETA}}$ and identify $c_{\text{ax}}^2 \rightarrow c_\phi^2$ in this limit (see Ref. [45]). The combination of the two limits produces the full model for the sound speed in Eq. (20).

The specific value for the phase of the background KG oscillations around the ETA as a function of m/H is also of interest. Since the background density is determined by the square of the field, the relevant quantity is

$$2\beta = \frac{m}{H} - \frac{3}{4}\pi, \quad (w_T = 1/3). \quad (\text{B11})$$

This determines the phase of the switch during radiation domination.

After radiation domination, the true expansion history cannot be fully characterized by a constant w_T , so for switches that occur after radiation domination, these analytic solutions do not directly apply. Nonetheless, for w^{ETA} and c_s , the variation with w_T in Eqs. (B6) and (B7) suggest that the equation of state and sound speed at $k \rightarrow 0$ still scale as $(H/m)^2$ but with A_w and A_c that vary by order unity across matter radiation equality. This motivates the prescription used in our effective method in Eqs. (17) and (20) where they are taken to be adjustable quantities.

Beyond radiation domination we can still obtain a good analytic approximation for the phase by assuming w_T varies very slowly compared with the oscillations. For example at high $m/H \gg 1$, the n th peak in the energy density $\rho_{\text{ax}} a^{-3}$ should be located at

$$2\beta = \pi/2 + 2\pi(n - 1) \quad (\text{B12})$$

for some integer n according to Eq. (B1) and we seek a prescription for the value of the scale factor a_* or H_* at which these maxima occur. First we take the $f_{\text{DM}} \ll 1$ limit where

$$Ht = \frac{2}{3} \frac{y^2 - y - 2 + 2\sqrt{1+y}}{y^2}, \quad (\text{B13})$$

with

$$y \equiv \frac{a}{a_{\text{eq}}}, \quad w_T = \frac{1}{3(1+y)} \quad (\text{B14})$$

so as to obtain the phase from Eq. (B5) as

$$2\beta = \frac{m}{H^{\text{ETA}}} \left(\frac{4}{3} \frac{y^2 - y - 2 + 2\sqrt{1+y}}{y^2} \right) - \frac{1+y}{4+3y} 3\pi. \quad (\text{B15})$$

Finally, given a desired phase 2β , e.g. from Eq. (B12) at the switch, we invert this formula to find

$$\frac{m}{H_*^{\text{ETA}}} = \frac{3}{4} \frac{y^2}{y^2 - y - 2 + 2\sqrt{1+y}} \left(2\beta + \frac{1+y}{4+3y} 3\pi \right). \quad (\text{B16})$$

where the use of H_*^{ETA} allows us to generalize this algorithm for finite f_{DM} . In this case, we assume that m/H_*^{ETA} is sufficiently large that the estimation of y using a matter scaling of $\rho_{\text{ax}}^{\text{ETA}} \propto a^{-3}$ to the present applies.

Note that the $y \rightarrow \infty$ solution is

$$\lim_{y \rightarrow \infty} \frac{m}{H_*^{\text{ETA}}} = \frac{3}{2}\beta + \frac{3\pi}{4} \quad (\text{B17})$$

which, in combination with Eq. (B11) for $y \rightarrow 0$, bounds the intermediate range. For a specified value of β , AxIICAMB takes an initial zeroth order guess for m/H_* based on an interpolation between the radiation and matter dominated limits:

$$\frac{m}{H_*^{(0)}} = 2\beta + \frac{3\pi}{4} - \frac{\beta^2}{2(\beta + m/H_{\text{eq}})} \quad (\text{B18})$$

and iterates on m/H_* until convergence in β is reached with Eq. (B15).

In Fig. 23 we test this prescription for locating density peaks on the maximally difficult case of $f_{\text{DM}} = 1$ and a mass where the corresponding scale factor is near equality, $m = 10^{-26}$ eV. We compare the location of the peaks in $\rho_{\text{ax}} a^3$ and their prediction from this procedure for $2\beta = 4.5\pi, 6.5\pi, 8.5\pi$ and show that they closely match. The resulting values from Eq. (B16) are $m/H_*^{\text{ETA}} = 15.7, 21.3, 27.0$ respectively.

This technique applies to any value of β and we use this technique in AxIICAMB to choose a specific phase at the switch that minimizes CMB errors around equality (see Appendix E). It may also be useful in other approaches that minimize errors by choosing specific phases in the KG oscillations (e.g. [51]).

Appendix C: ETA construction

This appendix provides details on the explicit construction for the ETA algorithm corresponding to Secs. II B in the main text.

In a separate module prior to the usual CAMB Boltzmann-Einstein system for the perturbations we solve for the KG background field by adapting the axion background module from AXIONCAMB. This module supplies KG field solutions at the switch time, parameterized by H_*/m

$$\begin{aligned} \phi_* &\equiv \phi \Big|_{H_*/m}, \\ \phi'_* &\equiv \frac{H}{m} \frac{d\phi}{d\ln a} \Big|_{H_*/m}. \end{aligned} \quad (\text{C1})$$

and use the notation $' = d/d(mt)$ here and below. Given the auxiliary field equation (5) and the KG equation (1), the auxiliary variables must satisfy

$$\begin{aligned} \varphi''_c + 2\varphi'_s + 3\frac{H}{m}[\varphi'_c + \varphi_s] &= 0, \\ \varphi''_s - 2\varphi'_c + 3\frac{H}{m}[\varphi'_s - \varphi_c] &= 0, \\ \varphi_c &= \phi_*, \\ \varphi_s + \varphi'_c &= \phi'_*, \end{aligned} \quad (\text{C2})$$

where we implicitly assume the auxiliary variables and their derivatives are evaluated at the switch and drop the $*$ subscript for compactness. The boundary condition Eq. (6) eliminates the second derivatives as $\varphi''_c = \mathcal{A}\varphi'_c, \varphi''_s = \mathcal{A}\varphi'_s$, where

$$\mathcal{A} = \frac{1}{m} \left(-\frac{3}{2} H^{\text{ETA}} + \frac{d \ln H^{\text{ETA}}}{dt} \right), \quad (\text{C3})$$

and reduces the system (C2) to a linear algebraic relation which uniquely determines the 4 auxiliary variables

$$\begin{aligned} \varphi_c &= \phi_*, \\ \varphi'_c &= -\frac{3\frac{H_*}{m} [2\phi_* + (\mathcal{A} + 3\frac{H_*}{m}) \phi'_*]}{\mathcal{A}^2 + 3\mathcal{A}\frac{H_*}{m} + 4}, \\ \varphi_s &= \phi'_* - \varphi'_c, \\ \varphi'_s &= \frac{3\frac{H_*}{m} (\mathcal{A}\phi_* - 2\phi'_*)}{\mathcal{A}^2 + 3\mathcal{A}\frac{H_*}{m} + 4}. \end{aligned} \quad (\text{C4})$$

Note that H_* here is the instantaneous Hubble rate at the switch, and should be distinguished from H^{ETA} . To evaluate \mathcal{A} requires H^{ETA} and ETA equation-of-state at the boundary, since

$$\mathcal{A} = -\frac{1}{2} \frac{H^{\text{ETA}}}{m} \left[3 - \frac{H_0^2}{(H^{\text{ETA}})^2} \sum_i -3(1+w_i) \frac{\rho_i}{\rho_c} \right], \quad (\text{C5})$$

where ρ_c is the critical density today, and the sum is over all components, including the ULA, for which we take $w_{\text{ax}}^{\text{ETA}} = p_{\text{ax}}^{\text{ETA}}/\rho_{\text{ax}}^{\text{ETA}}$.

Notice that evaluating H^{ETA} and $w_{\text{ax}}^{\text{ETA}}$ both determine auxiliary variables through the boundary condition and also require the auxiliary variables for their construction. This is resolved via iteration, where H^{ETA} and $w_{\text{ax}}^{\text{ETA}}$ are initialized as H and $9(H/m)^2/8$ respectively,⁹ and updated by the resulting $\rho_{\text{ax}}^{\text{ETA}}$ in Eq. (10) as H^{ETA} and $p_{\text{ax}}^{\text{ETA}}/\rho_{\text{ax}}^{\text{ETA}}$, until convergence is achieved for w^{ETA} (which also implies convergence in H^{ETA}).

The auxiliary perturbation variables follow a similar logic as the background, only that the H^{ETA} and thus \mathcal{A} are already defined by the background. Specifically

$$\begin{aligned}\delta\varphi_c &= \delta\phi_*, \\ \delta\varphi'_c &= \frac{-2\mathcal{B} - (\mathcal{A} + 3\frac{H_*}{m})\mathcal{C}}{2(\mathcal{A}^2 + 3\mathcal{A}\frac{H_*}{m} + \frac{2k^2}{a_*^2 m^2} + 4)}, \\ \delta\varphi_s &= \delta\phi'_* - \delta\varphi'_c, \\ \delta\varphi'_s &= \frac{\mathcal{A}\mathcal{B} - \left(2 + \frac{k^2}{a_*^2 m^2}\right)\mathcal{C}}{2(\mathcal{A}^2 + 3\mathcal{A}\frac{H_*}{m} + \frac{2k^2}{a_*^2 m^2} + 4)},\end{aligned}\quad (\text{C6})$$

where

$$\begin{aligned}\mathcal{B} &= (\varphi_c - \varphi'_s)h'_* - 2\frac{k^2}{a_*^2 m^2}\delta\phi'_* + 6\frac{H_*}{m}\delta\phi_*, \\ \mathcal{C} &= (\varphi'_c + \varphi_s)h'_* + 2\frac{k^2}{a_*^2 m^2}\delta\phi_* + 6\frac{H_*}{m}\delta\phi'_*.\end{aligned}\quad (\text{C7})$$

The auxiliary variables are then used to define the ETA of the ULA stress energy tensor components [45]

$$\begin{aligned}\rho_{\text{ax}}^{\text{ETA}} &= \frac{m^2}{2} \left(\varphi_c^2 + \varphi_s^2 + \frac{\varphi'_c{}^2}{2} + \frac{\varphi'_s{}^2}{2} - \varphi_c\varphi'_s + \varphi_s\varphi'_c \right), \\ p_{\text{ax}}^{\text{ETA}} &= \frac{m^2}{2} \left(\frac{\varphi'_c{}^2}{2} + \frac{\varphi'_s{}^2}{2} - \varphi_c\varphi'_s + \varphi_s\varphi'_c \right), \\ \delta\rho_{\text{ax}}^{\text{ETA}} &= \frac{m^2}{2} [\varphi_s\delta\varphi'_c - \varphi_c\delta\varphi'_s + \delta\varphi'_c\varphi'_s + \delta\varphi'_s\varphi'_s \\ &\quad + \delta\varphi_s(2\varphi_s + \varphi'_c) + \delta\varphi_c(2\varphi_c - \varphi'_s)], \\ \delta p_{\text{ax}}^{\text{ETA}} &= \delta\rho_{\text{ax}}^{\text{ETA}} - m^2 [\delta\varphi_s\varphi_s + \delta\varphi_c\varphi_c], \\ (\rho u)_{\text{ax}}^{\text{ETA}} &= \frac{mk}{2a} [\delta\varphi_c(\varphi_s + \varphi'_c) + \delta\varphi_s(-\varphi_c + \varphi'_s)].\end{aligned}\quad (\text{C8})$$

The ETA of the metric fluctuations η and σ follows once the partitioning of their responses to the KG oscillations are determined. In the main text, we used causality to specify this division and here we empirically test it

⁹ This starting value is taken from Eq. (B6) under matter domination $w_T = 0$ since $w_{\text{ax}}^{\text{ETA}}$ would only affect the construction if the ULAs contributed substantially to the expansion rate. The choice does not affect our final results here due to our iteration procedure. Likewise Ref. [45] does not need to iterate since they focus on $m \gg 10H_{\text{eq}}$ where the switch is deep in the radiation-dominated epoch and $H^{\text{ETA}} \approx H$.

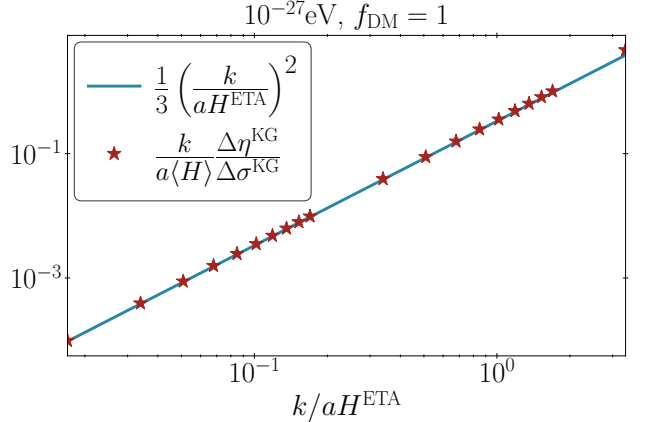


FIG. 24. Relative KG oscillation amplitude in the metric perturbations $\Delta\eta^{\text{KG}}$ and $\Delta\sigma^{\text{KG}}$ (red stars, see discussion around Eq. (C10)) compared with the prediction from the partitioning in Eq. (C11) (blue line) for $f_{\text{DM}} = 1$, $m = 10^{-27}$ eV.

against their numerical responses. To measure the amplitude of oscillations in η and σ , we examine the range $10 \lesssim m/H \lesssim 20$ in the KG system, and manually take the difference between a neighboring peak and trough of the KG oscillations

$$\Delta\{\sigma, \eta\}^{\text{KG}} \equiv \frac{1}{2} \left[\{\sigma, \eta\}_{\text{peak}} - \{\sigma, \eta\}_{\text{trough}} \right], \quad (\text{C9})$$

with the convention that these are positive definite quantities. We then construct

$$\frac{k}{a\langle H \rangle} \frac{\Delta\eta^{\text{KG}}}{\Delta\sigma^{\text{KG}}}, \quad (\text{C10})$$

where $\langle H \rangle$ is the background Hubble taken manually at the “node” point between the two and compare it to the model of Eq. (15) for the oscillation amplitude around the ETA

$$\frac{W}{1-W} = \frac{1}{3} \left(\frac{k}{aH^{\text{ETA}}} \right)^2, \quad (\text{C11})$$

The result of this test is plotted in Fig. 24 for $m = 10^{-27}$ eV, $f_{\text{DM}} = 1$, where we find good agreement across the k -modes ranging from 10^{-4} to 10^{-2} Mpc $^{-1}$, enclosing $k/aH^{\text{ETA}} \sim 1$, the most relevant scale range for the weighting. We have verified that this agreement is maintained across other masses in this regime ($m = 10^{-26} \sim 10^{-29}$ eV) and values of $f_{\text{DM}} \gtrsim 0.1$ where the oscillations can be accurately measured.

Appendix D: EFA and quasi-static equilibrium

In Sec. II C, the EFA for the ULA system is obtained by setting the EFA initial conditions by matching to ETA

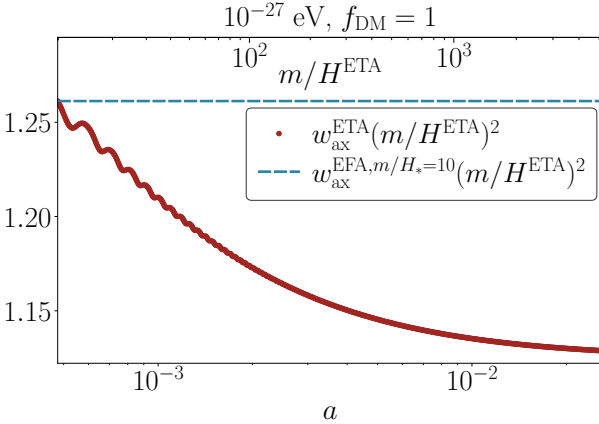


FIG. 25. Equation of state in EFA (blue dashed, switched at $m/H_* = 10$) and ETA (red dots) rescaled with $(m/H^{\text{ETA}})^2$ (top axis). Here $m = 10^{-27}$ eV, $f_{\text{DM}} = 1$.

variables at the switch, and also assigning values for the fluid equations of state $w_{\text{ax}}^{\text{EFA}}$ and c_{ax}^2 using Eqs. (17) and (20). The choices involved in this method set its accuracy, and differ from the prior approaches of AXIONCAMB and Ref. [45].

We now elaborate on these differences and their relationship to the quasi-static limit (QSL) of the sub-Jeans scale behavior of ULA perturbations. Put simply, a sharp switch from the KG w_{ax} to $w_{\text{ax}}^{\text{EFA}} = 0$ in AXIONCAMB does not maintain the QSL solution nor does the analytically motivated $w_{\text{ax}}^{\text{EFA}} = (3/2)(H/m)^2$ chosen in Ref. [45]. This becomes a spurious source of pressure-wave oscillations at the switch.

Consider the small scale limit of $k/am \gg 1$ and $k/aH \gg 1$. Under this condition, Eq. (2) yields

$$k^2 \delta \phi \approx -\frac{\dot{h}}{2} \dot{\phi}. \quad (\text{D1})$$

This closed-form non-dynamical (algebraic rather than differential) equation for $\delta \phi$ is the QSL solution and implies

$$k \rho_{\text{ax}} u_{\text{ax}} \equiv k(\rho_{\text{ax}} + p_{\text{ax}}) v_{\text{ax}} \approx -(\rho_{\text{ax}} + p_{\text{ax}}) \frac{\dot{h}}{2} \quad (\text{D2})$$

using Eq. (3). The source terms of the continuity equation (21) for $\delta \rho_{\text{ax}}$ cancel in this limit, effectively yielding an equation of hydrostatic equilibrium.

To understand this result, note that in synchronous gauge, gravitational effects are represented by the changes to the spatial metric through \dot{h} . The velocity v_{ax} is measured relative to free-fall and remains finite to counter \dot{h} when in equilibrium. More explicitly, in this limit \dot{h} is much larger than $\dot{\eta}$, and so Eq. (D2) becomes

$$v_{\text{ax}} \approx -\sigma. \quad (\text{D3})$$

Our switch conditions should respect this equilibrium, in addition to cycle-averaged momentum conservation

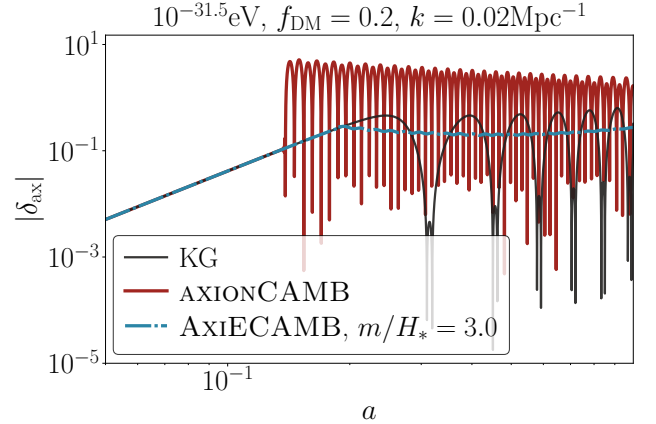


FIG. 26. ULA density fluctuation for $10^{-31.5}$ eV, $f_{\text{DM}} = 0.2$, at $k = 0.02 \text{ Mpc}^{-1}$. Plotted together are solutions from KG (gray), AXIONCAMB (red), and AxIECAMB set at the same $m/H_* = 3$ as AXIONCAMB (blue).

(i.e. $w_{\text{ax}}^{\text{ETA}} = w_{\text{ax}}^{\text{EFA}}$). As p_{ax} appears in the definition of the ULA momentum perturbation, jointly satisfying these constraints requires continuity in the cycle-averaged value of p_{ax} . Methods that instantaneously join p_{ax} to $w_{\text{ax}}^{\text{EFA}}$ $\rho_{\text{ax}}^{\text{EFA}}$ break equilibrium even if ρ_{ax} is taken to be continuous unless $w_{\text{ax}}^{\text{EFA}} = w_{\text{ax}}^{\text{ETA}}$. Since the instantaneous $p_{\text{ax}}/\rho_{\text{ax}}$ remains $O(1)$ as $m/H \rightarrow \infty$ this problem remains even for late switches (see Fig. 1). In our technique, the time-averaged velocity and momentum both remain continuous across the switch by choosing the equation of state $w_{\text{ax}}^{\text{EFA}} = w_{\text{ax}}^{\text{ETA}}$ by matching A_w . This differs from Ref. [45], where $A_w = 3/2$ was taken to be the predicted value of Eq. (B6) in radiation domination.

We illustrate this technique in Fig. 25, where w_{ax} is scaled to reflect the value of A_w . At $m/H_* = 10$, we equate $w_{\text{ax}}^{\text{EFA}} = w_{\text{ax}}^{\text{ETA}}$ and compare it to the discrete evaluation of the ETA at later times. Notice that the effective value of A_w decreases with time, as is expected from Eq. (B6) where $A_w = 9/8$ in matter domination. While some of this fractional evolution could be captured by Eq. (B6), the correction is small since $w_{\text{ax}}^{\text{EFA}}$ itself is small and decreasing as a^{-3} in the matter dominated limit. Our technique thus has the advantage of maintaining pressure continuity at the expense of a negligible error in the EFA equation state.

This advantage is illustrated in Fig. 26 where we compare the ULA density perturbation δ_{ax} output from AXIONCAMB to AxIECAMB for the same switch time set by the condition $m/H_* = 3$, using the same high-accuracy settings `accuracy_boost = 1_accuracy_boost = 3`, for $m = 10^{-31.5}$ eV, $f_{\text{DM}} = 0.2$, $k = 0.02 \text{ Mpc}^{-1}$. The KG solution is plotted for comparison. The sudden large oscillations result from a p_{ax} discontinuity in AXIONCAMB that violates the cancellation of $v_{\text{ax}}^{\text{EFA}}$ and \dot{h} . The continuity equation then generates a large spu-

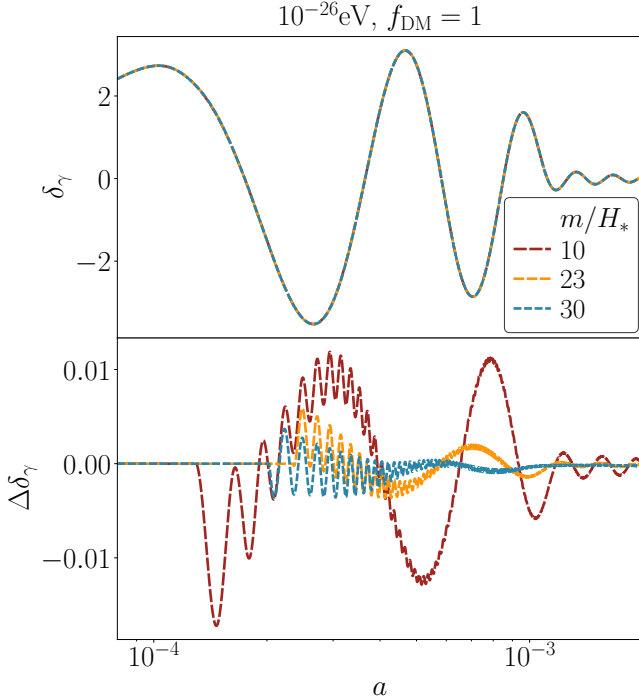


FIG. 27. Photon density perturbation (top) and the difference between the AxieCMB solution switched at various m/H_* values and the KG system solution (bottom) for $m = 10^{-26}$ eV, $f_{\text{DM}} = 1$ and $k = 0.1 \text{ Mpc}^{-1}$. At the phase-tuned switch of $m/H_* = 23$, the errors at recombination are reduced beyond even that of $m/H_* = 30$ and greatly reduced from the baseline of 10.

rious Jeans oscillation. This causes a large error in the ULA variables even at the present time. For the matter power spectrum, its impact is reduced by contributions from the cold dark matter and baryons (see Fig. 21). Our technique maintains a well-controlled $\delta_{\text{ax}}^{\text{EFA}}$ even at the same early switch $m/H_* = 3$ and provides accurate observables for any f_{DM} .

Appendix E: CMB implementation

We now elaborate on the two CMB-related issues discussed in Sec. II D: the choice of switch time m/H_* for masses $10^{-28} \lesssim m/\text{eV} \lesssim 10^{-25}$ and large f_{DM} , and the impact of additional CMB source terms due to discontinuities between KG and EFA at the switch.

The EFA of ULA and metric variables only removes the leading-order effect of the KG oscillations. Since the CMB is particularly sensitive to the epoch around equality, the next-to-leading-order effect produces $(8\pi G\rho_{\text{ax}}/H^2)\mathcal{O}(H_*^2/m^2)$ oscillatory responses to the KG oscillations in the photon density and velocity perturbations that are not time averaged and remain as artefacts after the switch that change the amplitude and phase of CMB acoustic oscillations.

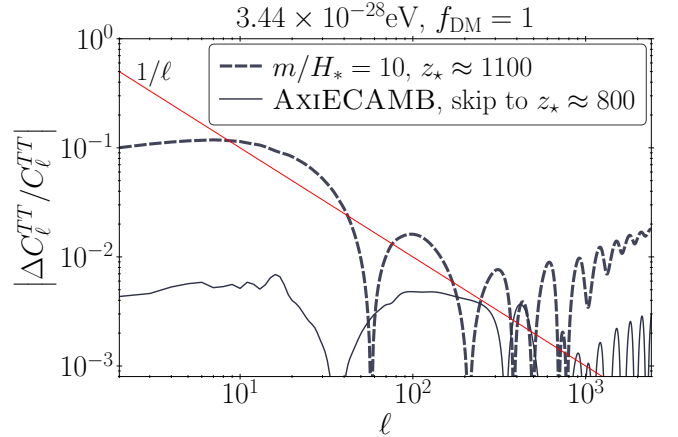


FIG. 28. C_ℓ^{TT} errors induced by placing the switch around recombination. The baseline $m/H_* = 10$ switch for $m = 3.44 \times 10^{-28}$ eV, $f_{\text{DM}} = 1$ is at $z_* \approx 1100$ whereas AxieCMB skips to $z_* \approx 800$. Errors compared with the high accuracy calculation are much larger than cosmic variance in the former.

We show an example in Fig. 27. In the top panel, we compare the KG solution (grey solid line) to ETA/EFA results for a switch at $m/H_* = 10$ (red dashed line) for the photon density perturbation δ_γ for $m = 10^{-26}$ eV, $f_{\text{DM}} = 1$ and $k = 0.1 \text{ Mpc}^{-1}$. The two agree to better than percent level accuracy and both exhibit the dominant photon acoustic oscillations. We show the error in the photon fluctuations, $\Delta\delta_\gamma$ (bottom panel), where the finer-scale oscillations in $\Delta\delta_\gamma$ after the switch reflect the continued photon response to KG oscillations that are removed in the EFA, rather than an EFA related error. More specifically, the discrepancy generated by instantaneously matching δ_γ at the switch instead of its time average gives rise to an error in the KG-induced δ_γ response, which then transfers to a phase and amplitude error in the subsequent baryon-photon acoustic oscillations. Once generated at the switch, this error does not decay away and its value at recombination is imprinted in C_ℓ^{TT} for the EFA.

This error is reducible with the technique of Appendix B since it originates from catching the KG oscillation at a particular phase. In particular, we can choose the best phase as well as raise m/H_* itself in this high sensitivity region. To demonstrate this in Fig. 27, we also show the $m/H_* = 23$ scenario (blue solid line), where the switch has been tuned to approximately minimize the errors in the acoustic oscillations. Notice that the errors are substantially less than the naive $(8\pi G\rho_{\text{ax}}/H^2)(H_*/m)^2$ scaling would imply, which we demonstrate with an example with an even higher value of $m/H_* = 30$ (yellow dotted line) that is not phase matched yet has a higher error.

The technique of Appendix B allows us to take this phase tuning in the 10^{-26} eV, $f_{\text{DM}} = 1$ case and apply it to other masses, k values, and switch epochs. Using Eq. (B15) we find that this best phase around $m/H_* = 20$

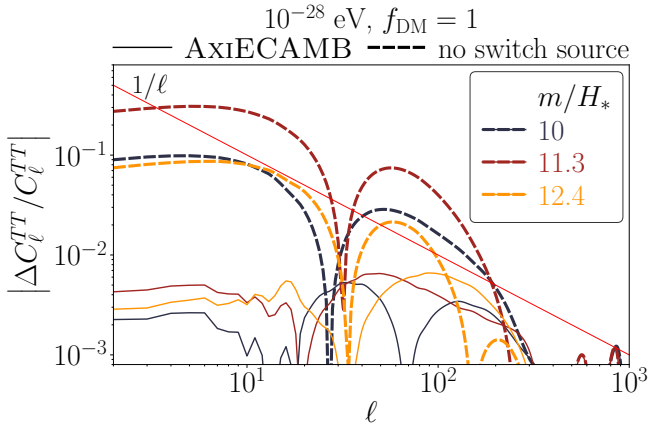


FIG. 29. C_ℓ^{TT} errors from omitting (dashed) or including (including) the switch sources (see Sec. IID) for $m = 10^{-28}$ eV and $f_{DM} = 1$ compared with the high accuracy solution. Omitting them generates larger than cosmic variance errors at low ℓ which are strongly dependent on the phase of the KG oscillation at m/H_* with the maximum and minimum around $m/H_* = 10$ shown here.

corresponds to

$$2\beta \approx 7.08\pi. \quad (\text{E1})$$

Finally using Eq. (B16), we take this value of 2β to predict the best m/H_*^{ETA} and iteratively solve for the corresponding m/H_* . While the tuning degrades away from $m = 10^{-26}$ eV, it suffices to improve the $10^{-27.5} \lesssim m/\text{eV} \lesssim 10^{-25}$ regime. Note that by tuning to 2β rather than m/H_* in the fiducial model we have automatically allowed for scalings of parameters away from their fiducial values.

Next we illustrate the reason for never allowing the switch to be in the recombination range $z_* \in (800, 1300]$. In Fig. 28, we show the specific mass where the baseline $m/H_* = 10$ would place $z_* = 1100$ and compare it to the AxIECAMB default of moving it to $z_* \approx 800$. The errors in the former case are larger than cosmic variance even at the intermediate $\ell \sim 10^2$ range and are not of the type that can be corrected by a θ_* shift. The high sensitivity to recombination of the CMB source function, which carries derivatives of the opacity $\dot{\mu}$ (see Eq. 27), makes skipping this redshift window important. We also increase the CMB source sampling density around recombination to account for the KG oscillation timescale when the switch is after recombination.

Lastly, we consider the impact of the switch sources discussed in Sec. IID. These sources account for the boundary terms from integration by parts of the original multipole sources in the construction of the total source. In Fig. 29 we show the effect of removing these switch sources for the case $m = 10^{-28}$ eV, $f_{DM} = 1$ and switches around our baseline $m/H = 10$. The effect of the switch source can be above the cosmic variance line and depends strongly on the phase of the ULA oscillation

at the switch. In Fig. 29, we highlight the best and worst cases around $m/H_* = 10$. Even though this $f_{DM} = 1$ model is far from observationally viable, the errors due to omitting the switch sources peak at $\Delta C_\ell / C_\ell \sim 0.3$, which is very large by modern CMB code standards. In Fig. 5, we show that the switch source is associated with a phase-dependent incomplete cancellation of the KG oscillations before the switch. With the switch sources included, AxIECAMB is accurate for all phases. The cancellation of the KG oscillations before the switch also requires very dense and symmetric source sampling right around the switch to guarantee accurate line-of-sight integration.

The switch itself is implemented using the standard CAMB switch mechanism which prevents any equation of motion from being integrated across the discontinuous boundary. This switch procedure guarantees that the equations on either side of the switch are solved separately and that evolution variables are assigned correctly at the switch epoch.

-
- [1] N. Aghanim *et al.* (Planck), *Astron. Astrophys.* **641**, A6 (2020), [Erratum: *Astron. Astrophys.* 652, C4 (2021)], arXiv:1807.06209 [astro-ph.CO].
- [2] S. Aiola *et al.* (ACT), *JCAP* **12**, 047 (2020), arXiv:2007.07288 [astro-ph.CO].
- [3] F. Ge *et al.* (SPT-3G), (2024), arXiv:2411.06000 [astro-ph.CO].
- [4] D. Rubin *et al.*, (2023), arXiv:2311.12098 [astro-ph.CO].
- [5] T. M. C. Abbott *et al.* (DES), *Astrophys. J. Lett.* **973**, L14 (2024), arXiv:2401.02929 [astro-ph.CO].
- [6] A. G. Adame *et al.* (DESI), (2024), arXiv:2404.03002 [astro-ph.CO].
- [7] T. M. C. Abbott *et al.* (DES), *Phys. Rev. D* **105**, 023520 (2022), arXiv:2105.13549 [astro-ph.CO].
- [8] C. Heymans *et al.*, *Astron. Astrophys.* **646**, A140 (2021), arXiv:2007.15632 [astro-ph.CO].
- [9] H. Miyatake *et al.*, *Phys. Rev. D* **108**, 123517 (2023), arXiv:2304.00704 [astro-ph.CO].
- [10] L. Breuval, A. G. Riess, S. Casertano, W. Yuan, L. M. Macri, M. Romaniello, Y. S. Murakami, D. Scolnic, G. S. Anand, and I. Soszyński, *Astrophys. J.* **973**, 30 (2024), arXiv:2404.08038 [astro-ph.CO].
- [11] W. L. Freedman, B. F. Madore, I. S. Jang, T. J. Hoyt, A. J. Lee, and K. A. Owens, (2024), arXiv:2408.06153 [astro-ph.CO].
- [12] N. Schöneberg, G. Franco Abellán, A. Pérez Sánchez, S. J. Witte, V. Poulin, and J. Lesgourgues, *Phys. Rept.* **984**, 1 (2022), arXiv:2107.10291 [astro-ph.CO].
- [13] E. Di Valentino, O. Mena, S. Pan, L. Visinelli, W. Yang, A. Melchiorri, D. F. Mota, A. G. Riess, and J. Silk, *Class. Quant. Grav.* **38**, 153001 (2021), arXiv:2103.01183 [astro-ph.CO].
- [14] P. Svrcek and E. Witten, *JHEP* **06**, 051 (2006), arXiv:hep-th/0605206 [hep-th].
- [15] J. P. Conlon, *JHEP* **05**, 078 (2006), arXiv:hep-th/0602233.
- [16] A. Arvanitaki, S. Dimopoulos, S. Dubovsky, N. Kaloper, and J. March-Russell, *Phys. Rev.* **D81**, 123530 (2010), arXiv:0905.4720 [hep-th].
- [17] M. Cicoli, M. Goodsell, and A. Ringwald, *JHEP* **10**, 146 (2012), arXiv:1206.0819 [hep-th].
- [18] M. J. Stott, D. J. E. Marsh, C. Pongkitivanichkul, L. C. Price, and B. S. Acharya, *Phys. Rev.* **D96**, 083510 (2017), arXiv:1706.03236 [astro-ph.CO].
- [19] N. Gendler, D. J. E. Marsh, L. McAllister, and J. Moritz, (2023), arXiv:2309.13145 [hep-th].
- [20] P. W. Graham, J. Mardon, and S. Rajendran, *Phys. Rev. D* **93**, 103520 (2016), arXiv:1504.02102 [hep-ph].
- [21] M. A. Amin, M. Jain, R. Karur, and P. Mocz, *JCAP* **08**, 014 (2022), arXiv:2203.11935 [astro-ph.CO].
- [22] J. A. Frieman, C. T. Hill, A. Stebbins, and I. Waga, *Phys. Rev. Lett.* **75**, 2077 (1995), arXiv:astro-ph/9505060 [astro-ph].
- [23] K. Choi, *Phys. Rev. D* **62**, 043509 (2000), arXiv:hep-ph/9902292.
- [24] D. J. E. Marsh and P. G. Ferreira, *Phys. Rev.* **D82**, 103528 (2010), arXiv:1009.3501 [hep-ph].
- [25] D. J. E. Marsh, *Phys. Rept.* **643**, 1 (2016), arXiv:1510.07633 [astro-ph.CO].
- [26] A. A. Klypin, A. V. Kravtsov, O. Valenzuela, and F. Prada, *Astrophys. J.* **522**, 82 (1999), arXiv:astro-ph/9901240.
- [27] W. J. G. de Blok, *Adv. Astron.* **2010**, 789293 (2010), arXiv:0910.3538 [astro-ph.CO].
- [28] M. Boylan-Kolchin, J. S. Bullock, and M. Kaplinghat, *Mon. Not. Roy. Astron. Soc.* **415**, L40 (2011), arXiv:1103.0007 [astro-ph.CO].
- [29] J. S. Bullock and M. Boylan-Kolchin, *Ann. Rev. Astron. Astrophys.* **55**, 343 (2017), arXiv:1707.04256 [astro-ph.CO].
- [30] W. Hu, R. Barkana, and A. Gruzinov, *Phys. Rev. Lett.* **85**, 1158 (2000), arXiv:astro-ph/0003365 [astro-ph].
- [31] L. Hui, J. P. Ostriker, S. Tremaine, and E. Witten, *Phys. Rev. D* **95**, 043541 (2017), arXiv:1610.08297 [astro-ph.CO].
- [32] P. Fox, A. Pierce, and S. D. Thomas, (2004), arXiv:hep-th/0409059.
- [33] V. Poulin, T. L. Smith, D. Grin, T. Karwal, and M. Kamionkowski, (2018), arXiv:1806.10608 [astro-ph.CO].
- [34] M.-X. Lin, G. Benevento, W. Hu, and M. Raveri, *Phys. Rev.* **D100**, 063542 (2019), arXiv:1905.12618 [astro-ph.CO].
- [35] K. K. Rogers, R. Hložek, A. Laguë, M. M. Ivanov, O. H. E. Philcox, G. Cabass, K. Akitsu, and D. J. E. Marsh, *JCAP* **06**, 023 (2023), arXiv:2301.08361 [astro-ph.CO].
- [36] K. Abazajian *et al.*, (2019), arXiv:1907.04473 [astro-ph.IM].
- [37] Ž. Ivezić *et al.* (LSST), *Astrophys. J.* **873**, 111 (2019), arXiv:0805.2366 [astro-ph].
- [38] LSST Science Collaboration *et al.*, arXiv e-prints , arXiv:0912.0201 (2009), arXiv:0912.0201 [astro-ph.IM].
- [39] R. Mandelbaum *et al.* (LSST Dark Energy Science), (2018), arXiv:1809.01669 [astro-ph.CO].
- [40] L. Amendola *et al.*, *Living Rev. Rel.* **21**, 2 (2018), arXiv:1606.00180 [astro-ph.CO].
- [41] A. Aghamousa *et al.* (DESI), (2016), arXiv:1611.00036 [astro-ph.IM].
- [42] R. Hložek, D. Grin, D. J. E. Marsh, and P. G. Ferreira, *Phys. Rev. D* **91**, 103512 (2015), arXiv:1410.2896 [astro-ph.CO].
- [43] B. Ratra, *Phys. Rev. D* **44**, 352 (1991).
- [44] T. Cookmeyer, D. Grin, and T. L. Smith, *Phys. Rev. D* **101**, 023501 (2020), arXiv:1909.11094 [astro-ph.CO].
- [45] S. Passaglia and W. Hu, *Phys. Rev. D* **105**, 123529 (2022), arXiv:2201.10238 [astro-ph.CO].
- [46] C.-B. Chen and J. Soda, *JCAP* **06**, 049 (2023), arXiv:2303.00999 [astro-ph.CO].
- [47] D. Blas, J. Lesgourgues, and T. Tram, *JCAP* **1107**, 034 (2011), arXiv:1104.2933 [astro-ph.CO].
- [48] M. Baryakhtar, O. Simon, and Z. J. Weiner, *Phys. Rev. D* **110**, 083505 (2024), arXiv:2405.10358 [astro-ph.CO].
- [49] L. A. Ureña López and A. X. Gonzalez-Morales, *JCAP* **1607**, 048 (2016), arXiv:1511.08195 [astro-ph.CO].
- [50] F. X. L. Cedeño, A. X. González-Morales, and L. A. Ureña López, *Phys. Rev. D* **96**, 061301 (2017), arXiv:1703.10180 [gr-qc].
- [51] L. A. Ureña López and F. X. Linares Cedeño, (2023), arXiv:2307.05600 [astro-ph.CO].
- [52] N. Aghanim *et al.* (Planck), *Astron. Astrophys.* **641**, A6 (2020), arXiv:1807.06209 [astro-ph.CO].

- [53] C.-P. Ma and E. Bertschinger, *Astrophys. J.* **455**, 7 (1995), arXiv:astro-ph/9506072 [astro-ph].
- [54] W. Hu, C.-T. Chiang, Y. Li, and M. LoVerde, *Phys. Rev. D* **94**, 023002 (2016), arXiv:1605.01412 [astro-ph.CO].
- [55] W. Hu, *Astrophys. J.* **506**, 485 (1998), arXiv:astro-ph/9801234 [astro-ph].
- [56] J. Lesgourgues and T. Tram, *JCAP* **09**, 032 (2014), arXiv:1312.2697 [astro-ph.CO].
- [57] W. Hu, U. Seljak, M. J. White, and M. Zaldarriaga, *Phys. Rev. D* **57**, 3290 (1998), arXiv:astro-ph/9709066.
- [58] U. Seljak and M. Zaldarriaga, *Astrophys. J.* **469**, 437 (1996), arXiv:astro-ph/9603033 [astro-ph].
- [59] J. Lesgourgues, (2011), arXiv:1104.2932 [astro-ph.IM].
- [60] D. J. Eisenstein, W. Hu, and M. Tegmark, *Astrophys. J.* **518**, 2 (1999), arXiv:astro-ph/9807130 [astro-ph].
- [61] K. K. Rogers and H. V. Peiris, *Phys. Rev. Lett.* **126**, 071302 (2021), arXiv:2007.12705 [astro-ph.CO].
- [62] L. Amendola and R. Barbieri, *Phys. Lett. B* **642**, 192 (2006), arXiv:hep-ph/0509257.